SISSA

PAPER • OPEN ACCESS

The effects of relativistic hidden sector particles on the matter power spectrum

To cite this article: Himanish Ganjoo *et al* JCAP01(2023)004

View the article online for updates and enhancements.

The effects of relativistic hidden sector particles on the matter power spectrum

Himanish Ganjoo,[a,b,c,*] **Adrienne L. Erickcek,**[d] **Weikang Lin**[e] **and Katherine J. Mack**[a,c]

[a]Department of Physics, North Carolina State University,
Raleigh, NC 27695, U.S.A.

[b]Department of Physics and Astronomy, University of Waterloo,
Waterloo, ON, N2L 3G1, Canada

[c]Perimeter Institute of Theoretical Physics,
31 Caroline St. N., Waterloo, ON, N2L 2Y5, Canada

[d]Department of Physics and Astronomy, University of North Carolina at Chapel Hill,
Phillips Hall CB 3255, Chapel Hill, NC 27599, U.S.A.

[e]Tsung-Dao Lee Institute (TDLI) and School of Physics and Astronomy,
Shanghai Jiao Tong University,
Shengrong Road 520, 201210 Shanghai, P.R. China

E-mail: hganjoo@ncsu.edu, erickcek@physics.unc.edu, weikanglin@sjtu.edu.cn,
kmack@perimeterinstitute.ca

*Corresponding author.

Abstract. If dark matter resides in a hidden sector minimally coupled to the Standard Model, another particle within the hidden sector might dominate the energy density of the early universe temporarily, causing an early matter-dominated era (EMDE). During an EMDE, matter perturbations grow more rapidly than they would in a period of radiation domination, which leads to the formation of microhalos much earlier than they would form in standard cosmological scenarios. These microhalos boost the dark matter annihilation signal, but this boost is highly sensitive to the small-scale cut-off in the matter power spectrum. If the dark matter is sufficiently cold, this cut-off is set by the relativistic pressure of the particle that dominates the hidden sector. We determine the evolution of dark matter density perturbations in this scenario, obtaining the power spectrum at the end of the EMDE. We analyze the suppression of perturbations due to the relativistic pressure of the dominant hidden sector particle and express the cut-off scale and peak scale for which the matter power spectrum is maximized in terms of the properties of this particle. We also supply transfer functions to relate the matter power spectrum with a small-scale cut-off resulting from the pressure of the dominant hidden sector particle to the matter power spectrum that results from a cold hidden sector. These transfer functions facilitate the quick computation of accurate matter power spectra in EMDE scenarios with initially hot hidden sectors and allow us to identify which models significantly enhance the microhalo abundance.

Contents

1 Introduction

Recent null results for WIMP dark matter in direct detection experiments [1–3] and collider searches [4–13] have prompted interest in theories in which dark matter lives in a hidden sector only weakly coupled to the Standard Model [14–19]. In several hidden sector theories, long-lived massive particles dominate the energy content of the universe prior to Big Bang Nucleosynthesis (BBN), leading to an early matter-dominated era (EMDE) [20–28]. An EMDE enhances small-scale density perturbations in dark matter because subhorizon dark matter perturbations grow linearly with scale factor during matter domination, as opposed to the logarithmic growth that occurs during radiation domination [29–32]. This growth can lead to the formation of dense sub-Earth-mass microhalos long before structures are expected to form in scenarios without an EMDE [29, 30, 32].

Although these microhalos do not affect the large-scale structure of the universe, they boost dark matter (DM) annihilation rates, potentially producing detectable gamma-ray signals [32–35]. The DM annihilation signal is highly sensitive to the small-scale cut-off in the matter power spectrum because the cut-off scale sets the formation times and central

densities of the microhalos that form due to an EMDE [32, 35, 36]. For instance, changing the cut-off scale by a factor of two causes the DM annihilation boost to increase by two orders of magnitude [35]. Therefore, an accurate calculation of this small-scale cut-off is key to observationally constraining scenarios with an EMDE. In this work, we determine the small-scale cut-off scale that results from the relativistic pressure of the particle that dominates the hidden sector.

If the particle that dominates the energy density of the universe during the EMDE is initially relativistic, the growth of density perturbations is inhibited for modes that enter the horizon while the particle has significant pressure. We obtain exact solutions of the evolution of perturbations during an EMDE caused by a massive particle (which we call Y) in the hidden sector. We include the process by which this particle transitions from relativistic to nonrelativistic behavior before dominating the energy content of the universe. While perturbation equations for a relativistic hidden sector particle have been solved previously for a single set of parameters [21], we provide analytical expressions for the power spectrum peak and cut-off scales in terms of the statistics of the Y particles and the initial ratio of densities of Y and Standard Model (SM) particles. It is also possible that the Y particle experiences cannibalistic number-changing interactions that alter the evolution of its pressure; the resulting cut-off to the matter power spectrum was computed in refs. [26, 28]. Our analysis of how the Y particle generates a cut-off in the matter power spectrum in the absence of such interactions completes our understanding of how the pressure of the particle that dominates the energy density during the EMDE inhibits the growth of dark matter perturbations during the EMDE.

We provide fitting forms for transfer functions between the cases with a hot and cold hidden sector. These transfer functions facilitate the easy computation of the power spectrum cut-off caused by the pressure suppression of density perturbations. We also consider how our transfer functions change the boost factor calculations presented in ref. [34] (hereafter B19), in which the cut-off in the power spectrum was taken to be a Gaussian function of wavenumber with the cut-off scale set as the horizon scale when the mass of the dominant hidden sector particle is equal to the hidden sector temperature. Finally, we use our transfer functions to determine which EMDE scenarios generate observable enhancements to the microhalo population.

This paper is organized as follows. In section 2, we study the evolution of the different components of the universe in our model, including the density, sound speed and equation of state of the Y particles as they transition from being relativistic to nonrelativistic. In section 3, the evolution of the density perturbations in the Y particles and dark matter before, during, and after the EMDE is determined, and the suppression of perturbation growth due to the pressure of the Y particles is analyzed. In section 4, we present expressions for the wavenumber of the peak scale, for which the matter power spectrum is maximized. In section 5, we provide fitting forms for transfer functions for the computation of the matter power spectrum in scenarios with an initially relativistic particle dominating the hidden sector. Section 6 presents calculations of the dark matter annihilation boost and the power spectrum peak height using our transfer functions; we also discuss prospects for detecting the microhalos generated in EMDE cosmologies. Our results are summarized in section 7. The full calculation of the density, pressure, and sound speed of the Y particles is presented in appendix A. Appendix B contains the derivations of several relations between the parameters that describe the EMDE and the properties of the Y particle. The equations that govern the evolution of perturbations and their initial conditions are detailed in appendix C. Finally,

we provide an online application for computing EMDE-enhanced power spectra with the accurate small-scale cut-off that is described in appendix D. This paper uses natural units throughout, in which $c = \hbar = k_B = 1$.

2 Evolution of the homogeneous background

Our model considers a universe with three components: dark matter X; the thermal bath of relativistic SM particles, which we call radiation (denoted by the subscript R); and a particle Y with mass m that decays into SM particles. X and Y live in a hidden sector that is thermally decoupled from the Standard Model and has its own temperature T_{hs}. The Y particles are initially relativistic but transition to nonrelativistic behavior as the temperature of the hidden sector decreases. We assume that the X particles have frozen out before our calculations begin and are nonrelativistic with $m_X \gg T_{hs}$ and $\rho_X(a) \propto a^{-3}$.

We first establish the evolution of the homogeneous energy densities of the various components of our model. We begin our calculations at scale factor a_i, which is chosen such that $T_{hs,i} \equiv T_{hs}(a_i) = 300m$, so that the Y particles are initially relativistic. The initial SM density is set by the parameter $\eta \equiv \rho_R(a_i)/\rho_Y(a_i)$. The Y particles are weakly coupled to the SM particles with a decay rate Γ. Such couplings of the hidden sector to the Standard Model can arise via various renormalizable interactions, including the lepton portal [14, 37], the Higgs portal [14, 38, 39], and the vector portal [14, 40]. To obtain the evolution of the energy densities of these three components, the coupled equations for ρ_X, ρ_Y and ρ_R are solved numerically:

$$\dot{\rho}_Y + 3H(1 + w_Y)\rho_Y = -\Gamma m n_Y; \tag{2.1a}$$

$$\dot{\rho}_R + 4H\rho_R = \Gamma m n_Y; \tag{2.1b}$$

$$\dot{\rho}_X + 3H\rho_X = 0, \tag{2.1c}$$

where overdots denote d/dt and $H \equiv \dot{a}/a$. In eq. (2.1a), n_Y is the number density of Y particles, and w_Y is their time-varying equation of state parameter, defined as the ratio between pressure and density, $w_Y \equiv P_Y/\rho_Y$. The time evolution of w_Y encodes the transition from relativistic to nonrelativistic behavior for the Y particles, which we solve for exactly; the process is detailed in appendix A. The terms on the r.h.s. of eqs. (2.1a) and (2.1b) depend on $m n_Y$ instead of ρ_Y because the longer lab-frame lifetimes of faster particles compensate for the higher energies released by their decays [28]. We assume that X and Y particles are coupled only gravitationally, with no momentum exchange between the two species. However, the effects of additional couplings are discussed in section 4.1.

Figure 1 shows the solutions to eqs. (2.1) for a chosen set of parameters. The transition from $\rho_Y(a) \propto a^{-4}$ to $\rho_Y \propto a^{-3}$ can be modeled by a broken power law with a pivot scale factor given by $a_p/a_i = b T_{hs,i}/m$ where b depends only on the statistics of the Y particles. We find that b is 2.70 for bosons and 3.15 for fermions; these values of b are derived in appendix A. It follows from eq. (2.1b) that $\rho_R \propto g_*(T)T^4 \propto a^{-4}$ when $\Gamma m n_Y \ll H\rho_R$, where $g_*(T)$ is the relativistic degrees of freedom contributing to the energy density of relativistic SM particles. However, all our analytical results assume that entropy is conserved in the visible sector when $\Gamma m n_Y \ll H\rho_R$, so that $g_{*S}(T)a^3T^3$ is constant, where g_{*S} is the relativistic degrees of freedom contributing to the entropy density of the SM bath. When $\Gamma m n_Y$ exceeds $H\rho_R$, $\rho_R \propto a^{-3/2}$ due to the entropy injection from the decay of the Y particles into the visible sector. After the Y particles decay away, $\rho_R \propto a^{-4}$ again.
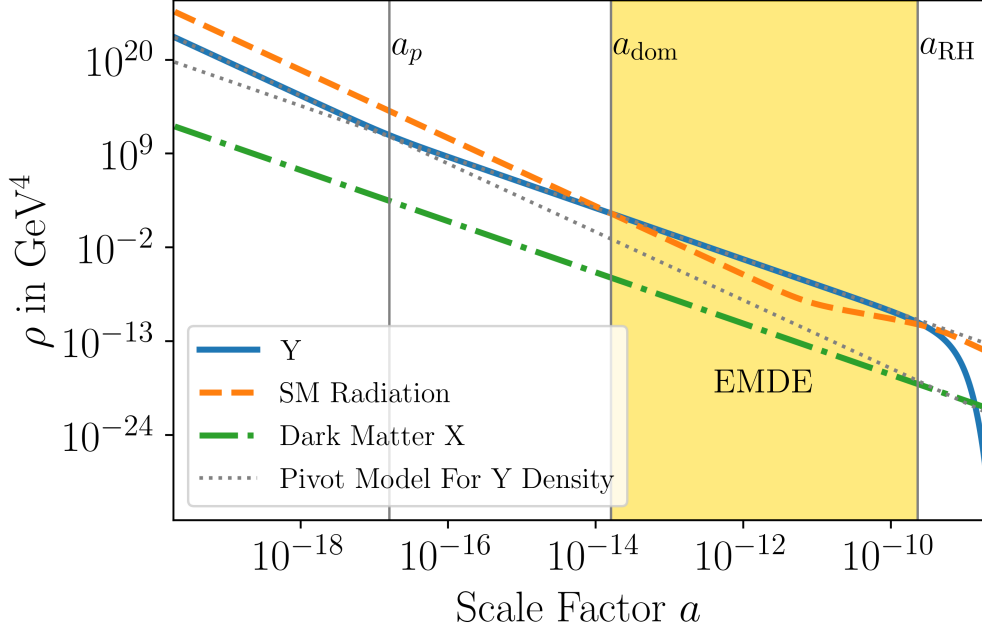
Figure 1. The background evolution of the energy densities of the Y particles, SM radiation and dark matter (X) as a function of scale factor, for parameters $m = 2\,\text{TeV}$ and $\eta = 1000$. The pivot scale factor a_p marks the transition from $\rho_Y \propto a^{-4}$ to $\rho_Y \propto a^{-3}$. The yellow shaded region shows the EMDE, which begins at the scale factor a_{dom}. At the end of the EMDE, ρ_Y rapidly decreases, and the universe becomes radiation dominated.

The EMDE, indicated by the yellow shaded region in figure 1, starts when ρ_Y exceeds ρ_R at the scale factor a_{dom}. We parameterize this point by the temperature of the SM radiation T_{dom}, so that $\rho_R(a_{\text{dom}}) = (\pi^2/30)g_*(T_{\text{dom}})T_{\text{dom}}^4$. We show in appendix B that T_{dom} can be expressed in terms of our model parameters as

$$g_*(T_{\text{dom}})^{\frac{1}{6}} T_{\text{dom}} = (fg)^{\frac{1}{4}} \left(\frac{m}{b}\right) g_*(T_i)^{-\frac{1}{12}} \eta^{-\frac{3}{4}}, \tag{2.2}$$

where g equals the number of degrees of freedom of the Y particles, T_i is the temperature of the SM radiation at a_i, and f is 1 if the Y particles are bosons and 7/8 if they are fermions.

The EMDE lasts until Γ/H becomes comparable to unity. After this point, the co-moving number density of the Y particles starts decreasing rapidly. Shortly thereafter, ρ_Y becomes negligible and the universe transitions to radiation domination. This transition, called *reheating*, is not an instantaneous process, but we find it useful to define a reheating temperature T_{RH} in terms of the decay rate as

$$\Gamma \equiv \sqrt{\frac{8\pi G}{3}\frac{\pi^2}{30}g_*(T_{\text{RH}})T_{\text{RH}}^4}\,, \tag{2.3}$$

which sets Γ equal to the Hubble rate in a purely radiation-dominated universe at temperature T_{RH}. It is also useful to define a_{RH} as the scale factor at which

$$\rho_Y(a_p)a_p^3 \equiv a_{\text{RH}}^3 \frac{\pi^2}{30}g_*(T_{\text{RH}})T_{\text{RH}}^4. \tag{2.4}$$

Note that T_{RH} is the quantity defined in eq. (2.3) and does not equal $T(a_{\text{RH}})$.

In our broken-power-law model, $\rho_Y(a_p)a_p^4 = \rho_Y(a_i)a_i^4$. Since the Y particles are relativistic at a_i, $\rho_Y(a_i) = fg(\pi^2/30)T_{\mathrm{hs,i}}^4$; it follows from the definition of a_{RH} that

$$\frac{a_{\mathrm{RH}}}{a_p} = \left[\frac{fg}{g_*(T_{\mathrm{RH}})}\right]^{\frac{1}{3}} \left[\frac{(m/b)}{T_{\mathrm{RH}}}\right]^{\frac{4}{3}}. \tag{2.5}$$

To relate a_{RH} to the scale factor today (a_0), we note that there is negligible transfer of entropy from the decay of the Y particles to the SM radiation for $a > 5a_{\mathrm{RH}}$. We find numerically that $T(5a_{\mathrm{RH}}) = 0.204T_{\mathrm{RH}}$ and use entropy conservation from $5a_{\mathrm{RH}}$ to a_0 to express

$$\frac{a_{\mathrm{RH}}}{a_0} = \frac{1}{1.02}\left[\frac{g_{*S}(T_0)}{g_{*S}(0.204T_{\mathrm{RH}})}\right]^{\frac{1}{3}}\left[\frac{T_0}{T_{\mathrm{RH}}}\right], \tag{2.6}$$

where T_0 is the temperature of radiation in the Universe today.

3 Evolution of perturbations

The Einstein equations are perturbed to obtain the equations for the evolution of the density contrast $\delta \equiv (\rho - \bar\rho)/\bar\rho$ (where $\bar\rho$ denotes homogeneous background density) and the velocity dispersion $\theta \equiv a\partial_i v^i$ for each fluid, where $v^i = dx^i/dt$. We work in the Newtonian gauge, in which the metric is given by

$$ds^2 = -(1 + 2\psi)dt^2 + a^2(t)(1 + 2\phi)(dx^2 + dy^2 + dz^2). \tag{3.1}$$

We neglect anisotropic stress and set $\psi = -\phi$. The perturbation equations and initial conditions are provided in appendix C.

Figure 2 shows the time evolution of $|\delta_i|/\Phi_0$, where Φ_0 is the primordial metric perturbation in a radiation-dominated universe and i denotes the three fluids in our model. Also shown is the evolution of the Y density perturbation if the Y particles were pressureless ($\delta_{Y,c}$). The left panel shows a mode that enters the horizon after the Y particles have become non-relativistic, with $T_{\mathrm{hs}}/m = 0.00018$ at horizon entry. In the absence of pressure, subhorizon density perturbations in Y grow logarithmically with scale factor during radiation domination and linearly during the EMDE. After the EMDE, radiation domination resumes and δ_X and δ_Y start growing logarithmically. For this mode, δ_Y coincides with $\delta_{Y,c}$ because the Y particles are already pressureless when the mode enters the horizon. In contrast, the right panel of figure 2 shows a mode that enters the horizon when the Y particles have significant pressure, with $w_Y = 0.14$ and $T_{\mathrm{hs}}/m = 0.21$ at horizon entry. For this mode, the growth of δ_Y is suppressed compared to that of $\delta_{Y,c}$ until the Y particles become pressureless. As a result, δ_Y starts linear growth later than $\delta_{Y,c}$ and $\delta_Y < \delta_{Y,c}$ at the end of the EMDE.

The right panel of figure 2 also shows how the evolution of δ_X is affected by the pressure of the Y particles. When the mode enters the horizon during radiation domination, δ_X starts to grow logarithmically with the scale factor. The pressure of the Y particles delays the onset of linear growth during the EMDE because the Y particles are not as clustered as they would have been if δ_Y had also grown logarithmically prior to the EMDE. Instead of growing linearly with scale factor throughout the EMDE, δ_X converges to δ_Y because the X particles fall into the gravitational wells generated by the Y particles. Due to this convergence, we will focus hereafter on analyzing the behavior of δ_Y.

To quantify which scales undergo growth suppression, we consider the continuity and Euler equations for the evolution of density and velocity perturbations in the Y particles
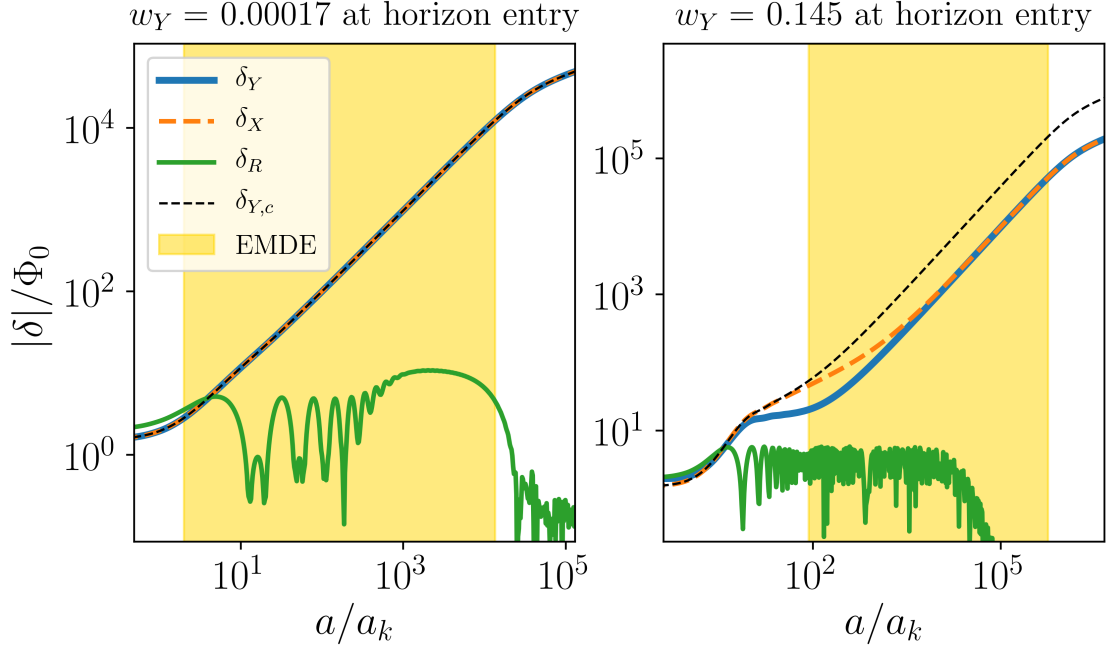
Figure 2. The evolution of perturbations for two modes, plotted as a function of a/a_k, where a_k is the scale factor of horizon entry for the mode. The mode in the left panel enters the horizon after the Y particles have become pressureless ($T_{\rm hs}/m = 0.00018$ at horizon entry); there is no suppression of δ_Y for this mode. The mode in the right panel enters the horizon when the Y particles have significant pressure ($T_{\rm hs}/m = 0.21$ at horizon entry) because of which δ_Y is suppressed compared to $\delta_{Y,c}$, the Y density perturbation if the Y particles are nonrelativistic.

along with the Poisson equation. Since the comoving number density of Y particles remains constant until $\Gamma \simeq H$ at the end of the EMDE, we can neglect the decay terms when the pressure of the Y particles is significant. We then have the following equations (taken from appendix C):

$$\frac{d\delta_Y}{da} = -\left(1 + w_Y\right)\left(\frac{\theta_Y}{a^2 H} + 3\frac{d\phi}{da}\right) - \frac{3}{a}(c_{sY}^2 - w_Y)\delta_Y, \tag{3.2a}$$

$$\frac{d\theta_Y}{da} = -\frac{1}{a}(1 - 3w_Y)\theta_Y - \frac{dw_Y}{da}\frac{\theta_Y}{1 + w_Y} + \frac{c_{sY}^2 k^2 \delta_Y}{(1 + w_Y)a^2 H} - \frac{k^2 \phi}{a^2 H}, \tag{3.2b}$$

$$a\frac{d\phi}{da} = -\left(1 + \frac{k^2}{3a^2 H^2}\right)\phi + \frac{4\pi G}{3H^2}(\rho_Y \delta_Y + \rho_R \delta_R), \tag{3.2c}$$

where $c_{sY}^2 = \delta P_Y / \delta \rho_Y$ is the sound speed of the Y particles (see appendix A). In eq. (3.2c), the contribution of the dark matter term ($\delta_X \rho_X$) on the r.h.s. is neglected because $\rho_X \ll \rho_Y$. Working in the subhorizon limit where $k \gg aH$ and using $H^2 = (8\pi G/3)(\rho_Y + \rho_R)$, eq. (3.2c) implies that

$$\left(\frac{k}{aH}\right)^2 \phi \simeq \frac{3}{2}\frac{\rho_Y \delta_Y + \rho_R \delta_R}{\rho_Y + \rho_R}. \tag{3.3}$$

To obtain the evolution of δ_Y, we neglect the derivative of ϕ in eq. (3.2a) as it is small compared to $\theta_Y/(a^2 H)$ and neglect the $(c_{sY}^2 - w_Y)\delta_Y$ term in eq. (3.2a) since $c_{sY}^2 - w_Y \approx 0$. Similarly, the term proportional to $(dw_Y/da)\theta_Y$ in eq. (3.2b) is neglected because dw_Y/da is
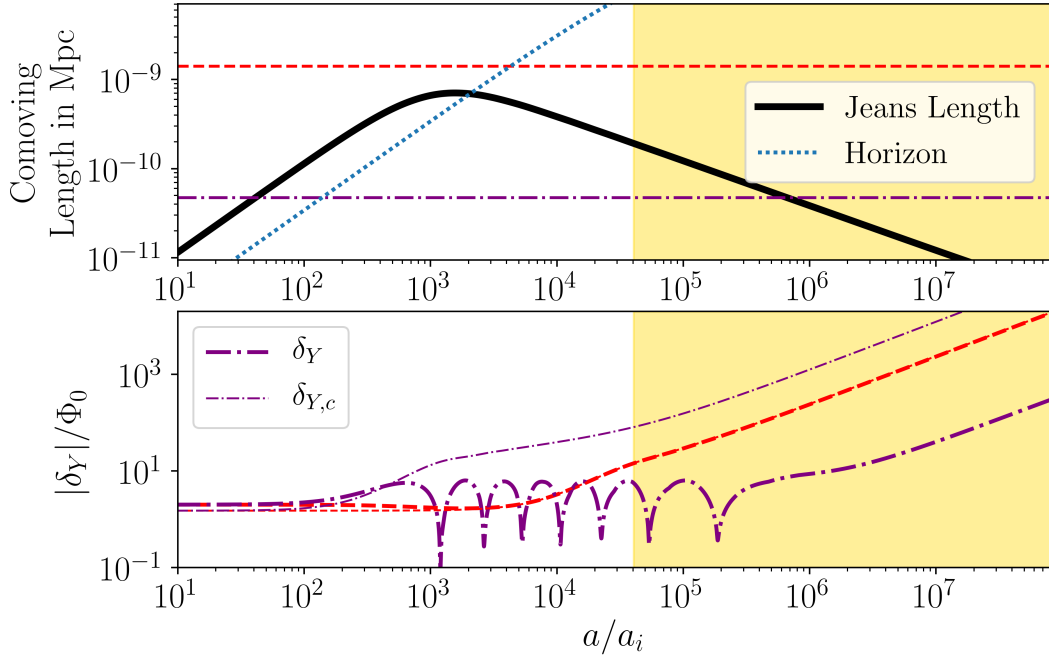
Figure 3. *Top*: the comoving wavelengths of two modes (horizontal lines), placed relative to the comoving Jeans length $\lambda_{\mathrm{J}} \equiv k_{\mathrm{J}}^{-1}$ and the comoving horizon $(aH)^{-1}$. The yellow shaded region is the EMDE. *Bottom*: the thick curves show the evolution of perturbations in the case where Y particles have relativistic pressure and the thin curves show the case where Y particles are treated as cold. The dashed curve corresponds to a scale that is always larger than the Jeans length, while the dot-dashed curve shows a scale that is much smaller than the Jeans length when it enters the horizon.

of the order of $(c_{sY}^2 - w_Y)$. Differentiating eq. (3.2a) with respect to a and using eqs. (3.2b) and (3.3) gives

$$\frac{d^2\delta_Y}{da^2} + \frac{1}{a}\left[\frac{d(a^2H)/da}{aH} + (1-3w_Y)\right]\frac{d\delta_Y}{da} + \frac{1}{a^2}\left[\frac{c_{sY}^2 k^2}{a^2 H^2} - \frac{3}{2}\frac{(1+w_Y)\rho_Y}{\rho_R+\rho_Y}\right]\delta_Y = \frac{3}{2a^2}\frac{(1+w_Y)\delta_R\rho_R}{\rho_R+\rho_Y}.$$
(3.4)

As figure 2 shows, δ_R begins oscillating shortly after the mode enters the horizon. The gravitational contribution of the $\delta_R\rho_R$ term on the r.h.s. of eq. (3.4) thus averages to zero and the term can be ignored. We can then express eq. (3.4) as

$$\frac{d^2\delta_Y}{da^2} + \frac{1}{a}\left[\frac{d(a^2H)/da}{aH} + (1-3w_Y)\right]\frac{d\delta_Y}{da} + \frac{c_{sY}^2}{(a^2H)^2}\left[k^2 - k_{\mathrm{J}}^2\right]\delta_Y = 0,$$
(3.5)

where we define the time-varying Jeans wavenumber

$$k_{\mathrm{J}}^2(a) \equiv \frac{3}{2}\frac{1+w_Y}{c_{sY}^2}\frac{\rho_Y}{\rho_R+\rho_Y}a^2H^2.$$
(3.6)

When the Y particles are relativistic, k_{J} is roughly proportional to a^{-1} because c_{sY}^2 is constant and $\rho_Y \propto a^{-4}$. As the Y particles become colder, k_{J} increases proportional to $a^{1/2}$ because $c_{sY}^2 \propto a^{-2}$ and $\rho_Y \propto a^{-3}$. This behavior is shown in the top panel of figure 3, where the black line shows the Jeans length $\lambda_{\mathrm{J}} \equiv k_{\mathrm{J}}^{-1}$.
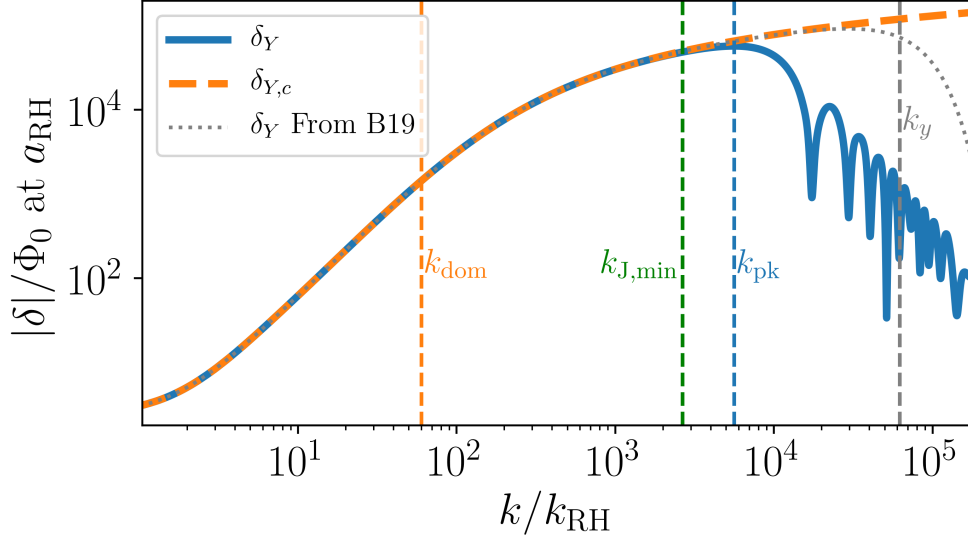
Figure 4. Density perturbations in Y at $a_{\rm RH}$ as a function of wavenumber, with $m = 5\,{\rm TeV}$, $T_{\rm RH} = 20\,{\rm MeV}$ and $\eta = 500$. The blue curve shows the solution in the case where the Y particles are initially relativistic (δ_Y). The orange dashed curve shows the case when they are treated as pressureless for the same $T_{\rm RH}$ ($\delta_{Y,c}$). The dot-dashed grey curve shows the estimate of $\delta_Y(k)$ used by B19: $\delta_{Y,c}(k) \exp[-k^2/(2k_y^2)]$, where k_y is the horizon wavenumber when $m = T_{\rm hs}$.

The sign of the coefficient of δ_Y in eq. (3.5) determines whether δ_Y grows or oscillates. Figure 3 illustrates the contrast between the growing and oscillating solutions. The top panel shows the comoving length scales (k^{-1}) corresponding to two different modes, plotted relative to the Jeans length. The bottom panel shows the time evolution of δ_Y for the two modes. The thin lines show the evolution of each mode if the Y particles are treated as nonrelativistic ($\delta_{Y,c}$). When $k < k_{\rm J}$ (so that $k^{-1} > \lambda_{\rm J}$), the coefficient of δ_Y in eq. (3.5) is negative, which leads to a growing solution for δ_Y. The mode represented by the red dashed line in figure 3 is such an example; its wavelength is always larger than the Jeans length. The bottom panel shows how the amplitude for this mode grows logarithmically with a during radiation domination and then grows linearly with a during the EMDE. In contrast, for the mode indicated by the purple dot-dashed line, the perturbation amplitude oscillates when $k^{-1} < \lambda_J$ and starts growing when $k^{-1} > \lambda_J$. Since δ_Y starts growing only when the Jeans length becomes smaller than the mode wavelength, δ_Y is reduced compared to $\delta_{Y,c}$.

The suppression of perturbation modes that enter the Jeans horizon is readily apparent in figure 4, which shows δ_Y and $\delta_{Y,c}$ evaluated at $a_{\rm RH}$ as a function of wavenumber scaled by $k_{\rm RH} \equiv a_{\rm RH}\Gamma$. If the Y particles are always pressureless, modes that enter the horizon before the EMDE grow logarithmically with a during radiation domination and then linearly with a during the EMDE, so that $\delta_{Y,c}(k > k_{\rm dom}, a_{\rm RH}) \propto \ln(k/k_{\rm dom})$, where $k_{\rm dom} \equiv a_{\rm dom}H(a_{\rm dom})$ is the horizon wavenumber at $a_{\rm dom}$. Modes that enter the horizon during the EMDE grow linearly with a from horizon entry until $a_{\rm RH}$, so that $\delta_{Y,c}(k_{\rm RH} < k < k_{\rm dom}, a_{\rm RH}) \propto (k/k_{\rm RH})^2$. The shape of $\delta_{Y,c}(k)$ after the EMDE only depends on the ratio $k_{\rm dom}/k_{\rm RH}$, which (as shown in appendix B) can be expressed in terms of our model parameters as

$$\frac{k_{\rm dom}}{k_{\rm RH}} = \sqrt{2} \left[\frac{gf}{g_*(T_{\rm RH})}\right]^{\frac{1}{6}} \left[\frac{g_*(T_i)}{g_*(T_{\rm dom})}\right]^{\frac{1}{6}} \left[\frac{(m/b)}{T_{\rm RH}}\right]^{\frac{2}{3}} \eta^{-\frac{1}{2}}. \tag{3.7}$$

If the Y particles are initially relativistic, the growth of perturbations is suppressed for scales close to or smaller than the maximum value of the Jeans length (shown by the wavenumber $k_{\rm J,min} = \lambda_{\rm J,max}^{-1}$ in figure 4). For these modes, δ_Y does not begin to grow until the Jeans length becomes smaller than the mode's wavelength. As a result, δ_Y at $a_{\rm RH}$ is increasingly suppressed compared to $\delta_{Y,c}$ as k increases, as the blue curve in figure 4 shows. The suppression leads to a peak in $\delta_Y(k)$ at the wavenumber $k_{\rm pk}$. For $k > k_{\rm pk}$, modes start growing not only later, but also at different points in the oscillation cycles of their amplitudes. This leads to an oscillation pattern in $\delta_Y(k)$ with a decaying envelope.

B19 modeled the suppression of modes that enter the horizon when the Y particle is relativistic by multiplying $\delta_{Y,c}(k)$ by $\exp[-k^2/(2k_y^2)]$, where k_y is the wavenumber of the mode that enters the horizon when $m = T_{\rm hs}$. In appendix B, we derive expressions for $k_y/k_{\rm dom}$ for a universe with $\eta > 1$. Using the expression for $k_y/k_{\rm dom}$ from eq. (B.14) with eq. (3.7) yields

$$\frac{k_y}{k_{\rm RH}} = b \left[\frac{gf}{g_*(T_{\rm RH})} \right]^{\frac{1}{6}} \left[\frac{g_*^3(T_i)}{g_{*y}g_*^2(T_{\rm dom})} \right]^{\frac{1}{6}} \left[\frac{(m/b)}{T_{\rm RH}} \right]^{\frac{2}{3}} (1 + \eta)^{\frac{1}{2}} , \qquad (3.8)$$

where $g_{*y} = g_*(T(a_y))$, with $a_y/a_i = T_{\rm hs,i}/m$. The cut-off used by B19 does not describe $\delta_Y(k)$ accurately: figure 4 shows that δ_Y falls off at smaller wavenumbers than k_y. In section 4, we derive the model dependence of the actual peak and cut-off scales of $\delta_Y(k)$.

4 The peak scale

In order to determine the observational signatures of an EMDE, it is necessary to evaluate the location and amplitude of the peak in the matter power spectrum, since this peak sets the masses, formation times, and central densities of the first microhalos [41, 42]. In this section, we provide expressions for the peak wavenumber $k_{\rm pk}$ for which $\delta_Y(k)/\Phi_0$ is maximized.

Due to the gravitational coupling between X and Y particles during the EMDE, the peak wavenumber of $\delta_X(k)$ is generally very close to that of $\delta_Y(k)$. However, the peaks are not exactly equal in all cases. The relative closeness of the peaks of $\delta_Y(k, a_{\rm RH})$ and $\delta_X(k, a_{\rm RH})$ depends on the duration of the EMDE, quantified by $k_{\rm dom}/k_{\rm RH}$. Figure 5 shows $\delta_X(k, a_{\rm RH})$ and $\delta_Y(k, a_{\rm RH})$ for three different EMDE durations. The leftmost panel shows a short EMDE with $k_{\rm dom}/k_{\rm RH} = 4.8$, in which case the peak wavenumbers of δ_Y and δ_X differ by 10% at the end of the EMDE. This difference arises because the EMDE is too short for δ_X and δ_Y to become equal for modes close to the peak wavenumbers. For scales smaller than the second peak in the left panel of figure 5, δ_Y oscillates throughout the EMDE because the Jeans length does not fall below the comoving wavelengths of these modes before $a_{\rm RH}$. As a result, the Y particles do not cluster and never exert a coherent gravitational pull on the X particles. The X particles drift during the EMDE and δ_X does not approach δ_Y. For longer EMDEs, the peaks of δ_X and δ_Y are nearly identical. The middle panel of figure 5 shows the case with $k_{\rm dom}/k_{\rm RH} = 17.7$, for which the peak wavenumbers of δ_X and δ_Y differ by 1.3%. For $k_{\rm dom}/k_{\rm RH} = 32.6$, this discrepancy between the peak scales falls to 0.4%. Therefore, the peak in δ_Y generally matches the corresponding peak in the matter power spectrum after the EMDE.

4.1 The effect of kinetic coupling in the hidden sector

Thus far, we have assumed that the Y particles and the dark matter X are coupled only gravitationally. In this section, we explore how scatterings between X and Y particles affect the peak amplitude and scale of δ_X and δ_Y.
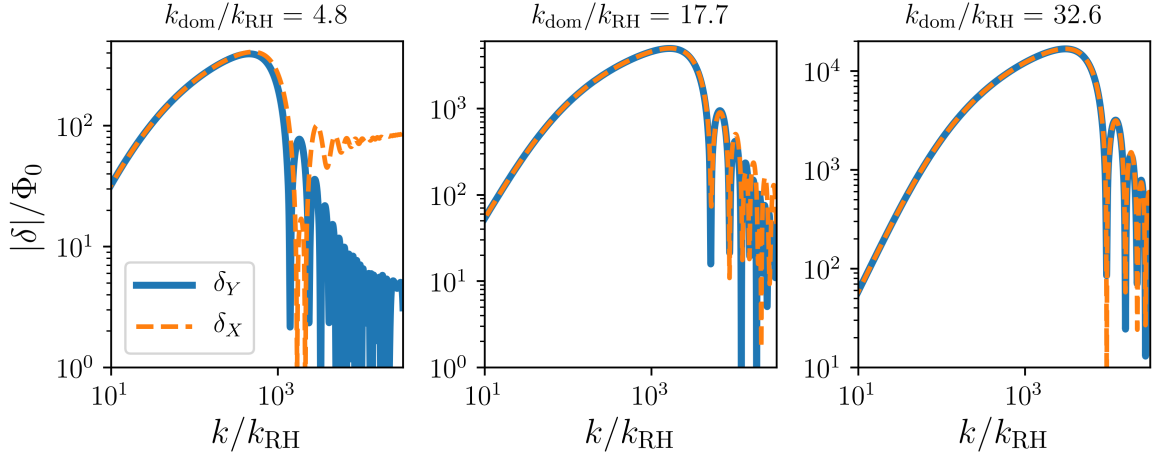
Figure 5. Density perturbations at $a_{\rm RH}$ as a function of wavenumber for three different EMDE durations.

If the X and Y particles are initially kept in kinetic equilibrium through a scattering process, the momentum transfer rate $(dp/dt)/p$ to the X particles from this scattering is given by $n_Y(m/m_X)\langle\sigma v\rangle$, where $\langle\sigma v\rangle$ is the velocity-averaged scattering cross section. This interaction modifies the Euler equation for the velocity perturbations in the dark matter [43]:

$$\theta'_X = -\theta_X - \frac{k^2}{aH}\phi + n_Y\frac{m}{m_X}\frac{\langle\sigma v\rangle}{H}(\theta_Y - \theta_X), \tag{4.1}$$

where the prime denotes $d/d\ln a$. The corresponding coupling term in the Euler equation for θ_Y is suppressed by a factor of ρ_X/ρ_Y and can be neglected. The coupling strength is parameterized by the scale factor of kinetic decoupling a_{kd}, which is defined by the relation $n_Y(a_{kd})\langle\sigma v\rangle = H(a_{kd})$.

To study the effect of this kinetic coupling, we consider three examples with $\eta = 300$, $k_{\rm dom}/k_{\rm RH} = 36$, and

1. no kinetic coupling between X and Y particles,

2. kinetic coupling with $a_{kd} = 0.5a_{\rm dom} = 150a_p$, such that the X and Y particles decouple before the EMDE starts but after the Y particles have become cold, and

3. kinetic coupling with $a_{kd} = 1.4a_{\rm RH}$, such that the X and Y particles remain coupled until after the Y particles have decayed into SM radiation.

While $n_Y\langle\sigma v\rangle \gg H$, $\theta_X \simeq \theta_Y$. As the hidden sector temperature decreases, the Y particles become nonrelativistic. In this regime, we can use the results of ref. [43] for the momentum transfer rate for the collision of two nonrelativistic particles and take $\langle\sigma v\rangle \propto \sqrt{T_{\rm hs}}$. For all these cases, we choose $m_X/m = 50$ so we can assume the DM particle is much heavier than the Y particle and $w_X \approx 0$. This ensures that the evolution of ρ_X is given by eq. (2.1c).

Figure 6 shows $\delta_Y(k, a_{\rm RH})$ and $\delta_X(k, a_{\rm RH})$ for the three cases mentioned above. The amplitude and the location of the first peak remain the same between the cases. Gravitational coupling during the EMDE is strong enough to make δ_X and δ_Y converge to within a 0.5% difference for wavenumbers close to $k_{\rm pk}$, even without kinetic coupling. The left panel
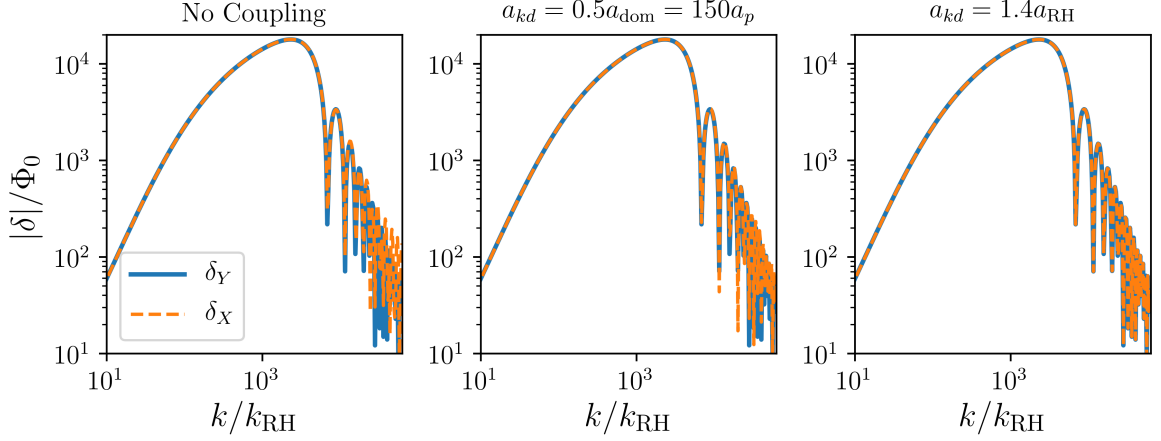
Figure 6. Density perturbations as a function of wavenumber, evaluated at $a_{\rm RH}$, with $\eta = 300$, $k_{\rm dom}/k_{\rm RH} = 36$ and $m_X/m = 50$. $\delta_X(k, a_{\rm RH})$ is plotted for cases with three different kinetic coupling strengths. The labels mark the scale factor of kinetic decoupling a_{kd} for the different coupling scenarios. For the case with no coupling (leftmost panel), the peak wavenumbers of δ_X and δ_Y differ by 0.4%.

of figure 6 also shows that δ_Y and δ_X differ for scales smaller than the peak scale in the case with no kinetic coupling. For these modes, δ_Y oscillates for a portion the EMDE, and the Y particles do not exert a coherent gravitational force on the DM until δ_Y stops oscillating. As a result, δ_X has not fully converged to δ_Y at $a_{\rm RH}$. Comparing the left and middle panels of figure 6, it is apparent that scatterings tie δ_X to δ_Y for these modes. Therefore non-gravitational interactions between the X and Y particles only serve to tighten the correspondence between δ_Y and δ_X and do not significantly affect the matter power spectrum.

4.2 Scenarios with initially subdominant Y particles

To derive an analytical expression for $k_{\rm pk}$ when the Y particle is initially subdominant ($\eta > 1$), we adopt the approach used to find the peak scale for cannibalistic hidden sector particles [28]. The peak scale enters the horizon after the Y particles have become nonrelativistic but before the onset of the EMDE. Since δ_R oscillates rapidly after the peak scale enters the horizon, the term proportional to $\delta_R \rho_R$ in eq. (3.4) does not affect the evolution of δ_Y. In addition, the term proportional to $\rho_Y/(\rho_Y + \rho_R)$ in the coefficient of δ_Y on the l.h.s. is negligible since $\rho_Y \ll \rho_R$ prior to the EMDE. Using entropy conservation in the visible sector, we can write $a^2 H = a_i^2 H(a_i)[g_*(T(a_i))/g_*(T(a))]^{1/6}$. The first term in the coefficient of $d\delta_Y/da$ in eq. (3.4) is then proportional to $d \ln g_*(T(a))/d \ln a$, which is negligible. We also set $1 + w_Y$ to unity, since w_Y is small compared to 1 and decreases as a^{-2} when the modes close to the peak scale enter the horizon. With these approximations, eq. (3.4) can be written as

$$\frac{d^2\delta_Y}{da^2} + \frac{1}{a}\frac{d\delta_Y}{da} + \frac{c_{sY}^2 k^2 \delta_Y}{(a^2 H)^2} = 0. \tag{4.2}$$

In appendix A, we present a piecewise model for $c_{sY}^2(a)$: $c_{sY}^2(a) = 0.33 a_{pc}^2/a^2$ for $a \gtrsim 1.4a_p$. Here, $a_{pc} = 1.43a_p$ for bosons and $1.41a_p$ for fermions, where $a_p = bT_{\rm hs,i}a_i/m$ is the pivot scale factor for broken power law that models $\rho_Y(a)$ and b is 2.70 for bosonic Y particles and 3.15 for fermionic Y particles. The different factors 1.41 and 1.43 reflect that

the Y particles have slightly different pressure for the same value of a/a_p if their statistics are different, which leads to the pivot points for their sound speed being at slightly different values of a/a_p. Since the peak scale enters the horizon when $a \gtrsim 1.4 a_p$, we can use $c_{sY}^2(a) = 0.33 a_{pc}^2/a^2$ in eq. (4.2), which then describes a simple harmonic oscillator in $\ln a$ with the k-dependent frequency $\omega_k = \beta a_p k g_a^{1/6}/(a_i^2 H_i g_i^{1/6})$, where $g_a = g_*(T(a))$, $g_i = g_*(T(a_i))$ and $\beta = 0.82$ for bosons and $\beta = 0.80$ for fermions. The factor of $g_a^{1/6}$ introduces a slight time-dependence into ω_k; we neglect this variation and set $g_a = g_k \equiv g_*(T(a_k))$ when solving eq. (4.3). The solution is

$$\delta_Y(k, a) = A_1 \sin\left[\omega_k \ln\left(A_2 \frac{a}{a_k}\right)\right]. \tag{4.3}$$

Since ω_k encodes the effect of the relativistic pressure of the Y particles, the expression for δ_Y for small ω_k should match the evolution of cold dark matter in radiation domination [44]: $\delta_X(a) = A\Phi_0 \ln(Ba/a_k)$ with $A = 9.11$ and $B = 0.594$. The coefficients A_1 and A_2 are determined by evaluating eq. (4.3) when $\omega_k \ll 1$ and matching it to this function. Prior to the EMDE, $\ln(a/a_k) \lesssim 10$ for modes near the peak scale, and the argument within the sine in eq. (4.3) is small compared to unity if $\omega_k \ll 1$. Using the approximation that $\sin x \simeq x$ for $x \ll 1$, it follows that $A_1 = A\Phi_0/\omega_k$ and $A_2 = B$.

The peak wavenumber $k_{\rm pk}$ can be found by maximizing the amplitude $\delta_Y(k, a_{\rm dom})$. Using the expressions for A_1 and A_2, we have

$$\delta_Y(k, a_{\rm dom}) = \frac{A\Phi_0}{\omega_k} \sin\left[\omega_k \ln\left(B\frac{a_{\rm dom}}{a_k}\right)\right] = \frac{A\Phi_0}{\omega_k} \sin\left[\omega_k \ln\left(\sqrt{2}B\left[\frac{g_k}{g_{\rm dom}}\right]^{\frac{1}{6}} \frac{k}{k_{\rm dom}}\right)\right], \tag{4.4}$$

where the second equality results from using the expression for $a_k/a_{\rm dom}$ in radiation domination from eq. (B.11). Neglecting the weak k-dependence of $(g_k/g_{\rm dom})^{1/6}$ and Φ_0 while setting the derivative of eq. (4.4) with respect to k equal to zero implies

$$\tan\left[\omega_{\rm pk} \ln\left(\frac{\sqrt{2}Bk_{\rm pk}}{k_{\rm dom}}\left[\frac{g_{\rm pk}}{g_{\rm dom}}\right]^{\frac{1}{6}}\right)\right] = \omega_{\rm pk}\left[1 + \ln\left(\frac{\sqrt{2}Bk_{\rm pk}}{k_{\rm dom}}\left[\frac{g_{\rm pk}}{g_{\rm dom}}\right]^{\frac{1}{6}}\right)\right]. \tag{4.5}$$

Since $k_{\rm pk}$ is an extremum of $\delta_Y(k)$, the tangent function on the l.h.s. is well-described by a Taylor expansion to second order around $k_{\rm pk}$. Using this expansion and solving the resulting equation for $k_{\rm pk}$ yields

$$\sqrt{2}B\frac{k_{\rm pk}}{k_{\rm dom}}\left[\frac{g_{\rm pk}}{g_{\rm dom}}\right]^{\frac{1}{6}} = \left[\frac{1.5}{r}W\left(\frac{2r}{3}\right)\right]^{-\frac{3}{2}}, \tag{4.6}$$

where W is the Lambert W-function and

$$r = \left[\frac{\sqrt{6}B}{\beta}\frac{a_i}{a_p}\frac{a_i H_i}{k_{\rm dom}}\left(\frac{g_i}{g_{\rm pk}}\right)^{\frac{1}{6}}\right]^{\frac{2}{3}}. \tag{4.7}$$

We express $a_i H_i/k_{\rm dom} = (a_{\rm dom}/(\sqrt{2}a_i))(g_{\rm dom}/g_i)^{1/6}$ (using eq. (B.11)) and use the definition of $a_{\rm dom}/a_p$ from eq. (B.5) to simplify the dependence of r on the model parameters. Substituting $B = 0.594$, we have

$$r = \left[\frac{0.95}{\beta}\left(\frac{g_i^2}{g_{\rm pk}g_{\rm dom}}\right)^{\frac{1}{6}}\eta\right]^{\frac{2}{3}}. \tag{4.8}$$

Finally, we use the expression for $k_y/k_{\rm dom}$ from eq. (B.14) to eliminate $k_{\rm dom}$ from eq. (4.6) and obtain

$$g_{\rm pk}^{\frac{1}{3}} \frac{k_{\rm pk}}{k_y} = (g_y g_{\rm dom})^{\frac{1}{6}} \frac{1.03}{\beta b} \sqrt{\frac{\eta}{1+\eta}} W^{-3/2} \left[0.77 \left(\frac{g_i^2}{g_{\rm pk} g_{\rm dom}} \right)^{\frac{1}{9}} \eta^{2/3} \right]. \qquad (4.9)$$

In the above expression, $g_{\rm pk} = g_*(T(a_{\rm pk}))$ and $g_{\rm dom} = g_*(T_{\rm dom})$. The r.h.s. of this expression includes an additional factor of 1.08 that brings the $k_{\rm pk}$ values into better agreement with those obtained from the numerical solutions of the perturbation equations.

To establish the relation between the peak scale and our model parameters, the peak scale can be rewritten in physical units. Using eqs. (2.3) and (2.6), and substituting $T_0 = 2.726$ K and $g_{*S}(T_0) = 3.91$, $k_{\rm RH} \equiv a_{\rm RH}\Gamma$ can be expressed as

$$\frac{k_{\rm RH}}{a_0} = 7.68 \left[\frac{g_*^{1/2}(T_{\rm RH})}{g_{*S}^{1/3}(0.204 T_{\rm RH})} \right] \left[\frac{T_{\rm RH}}{1 {\rm MeV}} \right] \times 10^3 \, {\rm Mpc}^{-1}. \qquad (4.10)$$

Using the definition of $k_y/k_{\rm RH}$ from eq. (3.8), the peak wavenumber is

$$\frac{k_{\rm pk}}{a_0} = \frac{0.9}{\beta} \left[\frac{fg}{b^4} \right]^{\frac{1}{6}} \left[\frac{g_*(T_{\rm RH})}{g_{*S}(0.2 T_{\rm RH})} \right]^{\frac{1}{3}} \left[\frac{T_{\rm RH}}{1 {\rm MeV}} \right]^{\frac{1}{3}} \left[\frac{m}{1 {\rm GeV}} \right]^{\frac{2}{3}} \frac{\eta^{\frac{1}{2}}}{W^{\frac{3}{2}}(0.77 \eta^{\frac{2}{3}})} \times 10^6 \, {\rm Mpc}^{-1}, \quad (4.11)$$

where we have ignored the variation of g_* before the EMDE for simplicity. In eq. (4.11), $k_{\rm pk}/a_0$ depends on $T_{\rm RH}$ because the reheat temperature determines when the EMDE ends and thus affects the expansion history of the Universe after the peak scale enters the horizon.

The points in figure 7 show $k_{\rm pk}/k_y$ for different η values as determined from the numerical solutions for the evolution of δ_Y, while the solid lines for $\eta > 1$ show $k_{\rm pk}/k_y$ from eq. (4.9) with $g_*(T) = 100$. The analytical expression explains the variation of $k_{\rm pk}/k_y$ with η and predicts the peak scale of $\delta_Y(k, a_{\rm RH})$ to within 3% of the numerically determined peak scale for $\eta \geq 100$. As η decreases, the peak scale enters the horizon closer to the pivot point of c_{sY}^2. Since the asymptotic late-time expression for c_{sY}^2 was used in the derivation of eq. (4.9), its prediction for $k_{\rm pk}$ diverges from the numerically determined peak wavenumber for $\eta < 100$.

4.3 Scenarios with initial Y-domination

If $\eta < 1$, ρ_R remains subdominant until reheating. The EMDE begins when ρ_Y starts decreasing proportional to a^{-3} at $a = a_p$, and this pivot also determines which modes are suppressed by the relativistic pressure of the Y particles. The numerical solutions to the perturbation equations for $\eta < 0.1$ indicate that $k_{\rm pk}$ enters the horizon while the Y particles are still relativistic ($a_{\rm pk} < a_p$) and that $a_{\rm pk} = a_p\sqrt{1+\eta}/\gamma$, where $\gamma = 2.055$ and 2.065 for bosonic and fermionic Y particles, respectively. The factor γ accounts for a slight difference between $k_{\rm pk}$ for fermionic and bosonic Y particles, which arises because the Y particles have slightly lower pressure at a given value of a/a_p if they are fermions compared to if they are bosons.

For $a < a_p$, $H(a) \propto a^{-2}$ and thus $k \propto a_k^{-1}$. Therefore, $k_{\rm pk}/k_p = \gamma/\sqrt{1+\eta}$. The wavenumber $k_p \equiv a_p H(a_p)$ can be obtained by expressing $H^2(a_p) = 8\pi G(\rho_Y(a_p) + \rho_R(a_p))/3 = 8\pi G \rho_Y(a_p)(1+\eta)/3$. In this expression, $\rho_Y(a_p)$ can be written using eq. (2.4) and the expression for $a_p/a_{\rm RH}$ from eq. (2.5). Finally, taking Γ from eq. (2.3),

$$\frac{k_p}{k_{\rm RH}} = \frac{a_p}{a_{\rm RH}} \frac{H(a_p)}{\Gamma} = \left[\frac{gf}{g_*(T_{\rm RH})} \right]^{\frac{1}{6}} \left[\frac{(m/b)}{T_{\rm RH}} \right]^{\frac{2}{3}} \sqrt{1+\eta}. \qquad (4.12)$$
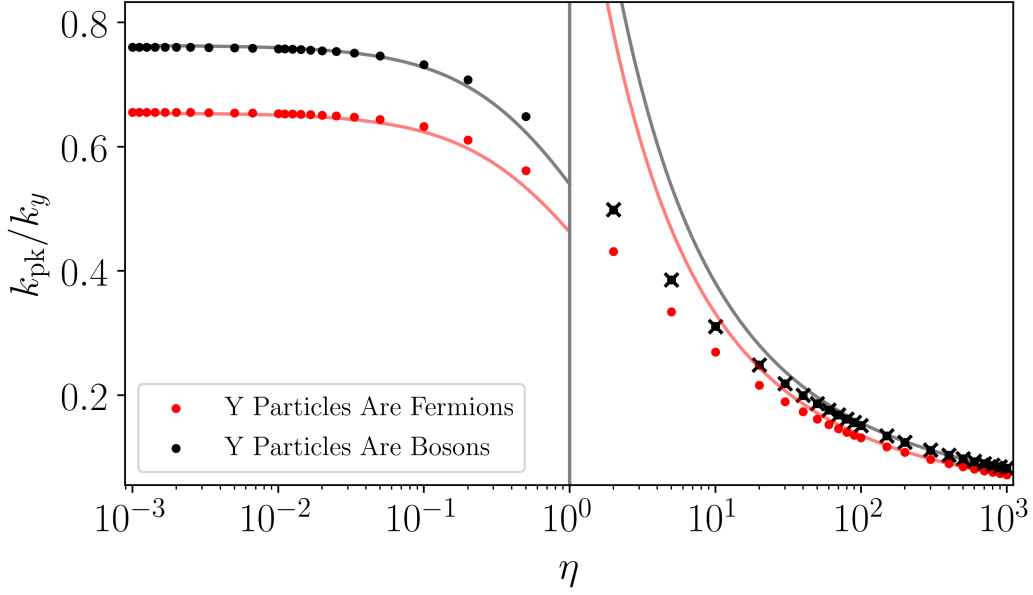
Figure 7. The peak wavenumber $k_{\rm pk}$ that maximizes $\delta_Y(k)$, scaled by k_y and plotted against η, the initial value of ρ_Y/ρ_R. The dots represent the $k_{\rm pk}$ determined from numerical data for $m = 2\,{\rm TeV}$ and the lines represent the analytical predictions for $k_{\rm pk}/k_y$, given by eq. (4.9) for $\eta > 1$ and by eq. (4.13) for $\eta < 1$. The plotted quantity $k_{\rm pk}/k_y$ depends only on η and the statistics of the Y particles. Different colors show cases with different Y particle statistics. This plot assumes $g_*(T) = g_{*S}(T) = 100$. The black crosses show $k_{\rm pk}/k_y$ for a boson Y particle for $m = 200\,{\rm GeV}$; they overlap with the black dots, confirming that $k_{\rm pk}/k_y$ is independent of m.

To express k_p in terms of k_y, we again use the scaling $k \propto a_k^{-1}$, which applies since $a_y < a_p$. Using this scaling yields $k_y/k_p = a_p/a_y = b$, so that

$$\frac{k_{\rm pk}}{k_y} = \frac{\gamma}{b}\frac{1}{\sqrt{1+\eta}}. \tag{4.13}$$

This prediction for $k_{\rm pk}/k_y$ is shown by the solid lines in figure 7 for $\eta < 1$. The value given by eq. (4.13) agrees with the peak scale to within 1% for $\eta < 0.1$. For $\eta > 0.1$, $k_{\rm pk}$ enters the horizon after c_{sY}^2 begins to decrease. This makes $k_{\rm pk}/k_y$ diverge from the prediction of eq. (4.13), which is valid for cases in which $c_{sY}^2(a_{\rm pk}) \simeq 1/3$. We can use eq. (4.12) and $k_y/k_p = b$ in conjunction with the definition of $k_{\rm RH}$ from eq. (4.10) to express $k_{\rm pk}$ in physical units as

$$\frac{k_{\rm pk}}{a_0} = 0.765\gamma \left[\frac{fg}{b^4}\right]^{\frac{1}{6}} \left[\frac{g_*(T_{\rm RH})}{g_{*S}(0.2T_{\rm RH})}\right]^{\frac{1}{3}} \left[\frac{T_{\rm RH}}{1{\rm MeV}}\right]^{\frac{1}{3}} \left[\frac{m}{1{\rm GeV}}\right]^{\frac{2}{3}} \times 10^6 \ {\rm Mpc}^{-1}. \tag{4.14}$$

5 Transfer functions

Solving the Boltzmann equations with an initially relativistic Y particle is computationally expensive. To facilitate the computation of the matter power spectrum in such hidden-sector cosmologies, we present analytical transfer functions that relate $\delta_Y(k)$ to $\delta_{Y,c}(k)$. The transfer function is defined as

$$T(k) \equiv \frac{\delta_Y(k)}{\delta_{Y,c}(k)}, \tag{5.1}$$
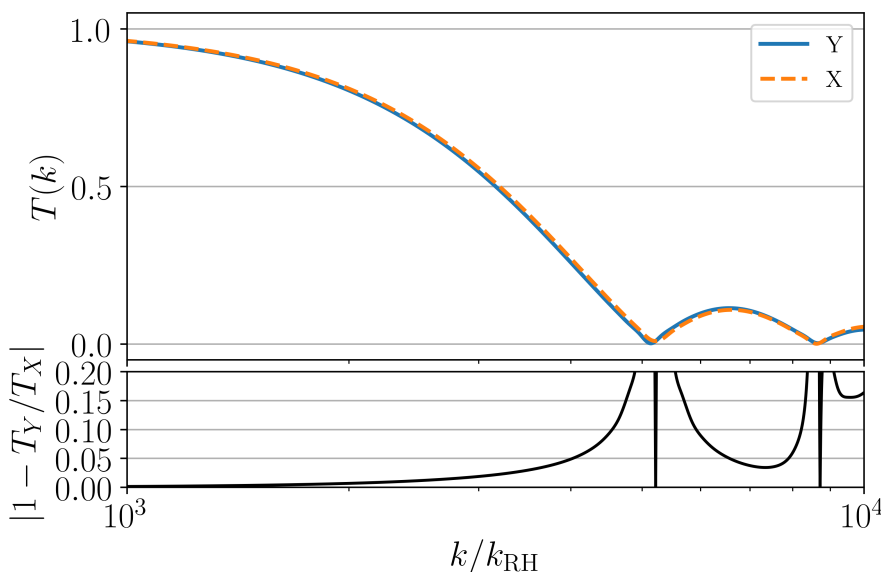
Figure 8. Comparing the transfer functions for X and Y perturbations for a case with $k_{\mathrm{dom}}/k_{\mathrm{RH}} = 17.7$. In the top panel, the solid line shows $T_Y = T(k)$ and the dashed line shows $T_X(k)$, while the bottom panel shows the relative difference between the two. The two transfer functions agree to within 5% for $T(k) \geq 0.25$.

where both $\delta_Y(k)$ and $\delta_{Y,c}(k)$ are evaluated at a_{RH}. For $\eta > 1$, we calculate $\delta_{Y,c}$ by setting $w_Y = c_{sY}^2 = 0$ and $\rho_Y(a_i) = \rho_Y(a_{\mathrm{dom}})(a_{\mathrm{dom}}/a_i)^3$, thus obtaining the evolution of density perturbations in cold particles for the same value of $\rho_Y(a)$ during the EMDE. If the relativistic Y particles initially dominate the universe, making the Y particles cold radically alters the evolution of the Hubble rate. To avoid conflating the effects of changing the Hubble rate with the effects of the Y particles' pressure, we use an analytical expression for $\delta_{Y,c}$ when computing $T(k)$ when $\eta < 1$, as described in section 5.2.

We focus on transfer functions for the Y density perturbations because they are less sensitive to the duration of the EMDE than transfer functions for DM perturbations would be. In most cases though, these transfer functions can be applied directly to the DM power spectrum. Figure 8 shows the correspondence of $T(k)$ and $T_X(k) \equiv \delta_X(k, a_{\mathrm{RH}})/\delta_{X,c}(k, a_{\mathrm{RH}})$ for $k_{\mathrm{dom}}/k_{\mathrm{RH}} = 17.7$ (where $\delta_{X,c}$ is the DM perturbation if the Y particles were pressureless). The bottom panel shows the relative error between T and T_X, which remains within 5% for $T(k) \geq 0.25$. Longer EMDEs lead to even closer agreement between $T_X(k)$ and $T(k)$.

We wish to fit a functional form to $T(k)$ that accurately models the transfer function. As can be seen in figure 9, the oscillatory pattern in $\delta_Y(k)$ for $k > k_{\mathrm{pk}}$ has a much lower amplitude than $\delta_Y(k_{\mathrm{pk}})$: δ_Y at the second peak scale is $\lesssim 0.25\delta_Y(k_{\mathrm{pk}})$ for both $\eta < 1$ and $\eta > 1$. Since perturbations at the scale of the first peak will collapse long before modes on smaller scales, we do not expect perturbations with $k > k_{\mathrm{pk}}$ to significantly affect the microhalo population. We will therefore prioritize accurately describing the first peak in $\delta_Y(k)$, while neglecting the smaller peaks at $k > k_{\mathrm{pk}}$. The function that best fits $T(k)$ and accurately describes the first peak in $\delta_Y(k)$ is

$$T(k) = \exp\left[-\left(\frac{k}{k_{\mathrm{cut}}}\right)^n\right],\tag{5.2}$$

where both n and k_{cut} are fitting parameters.
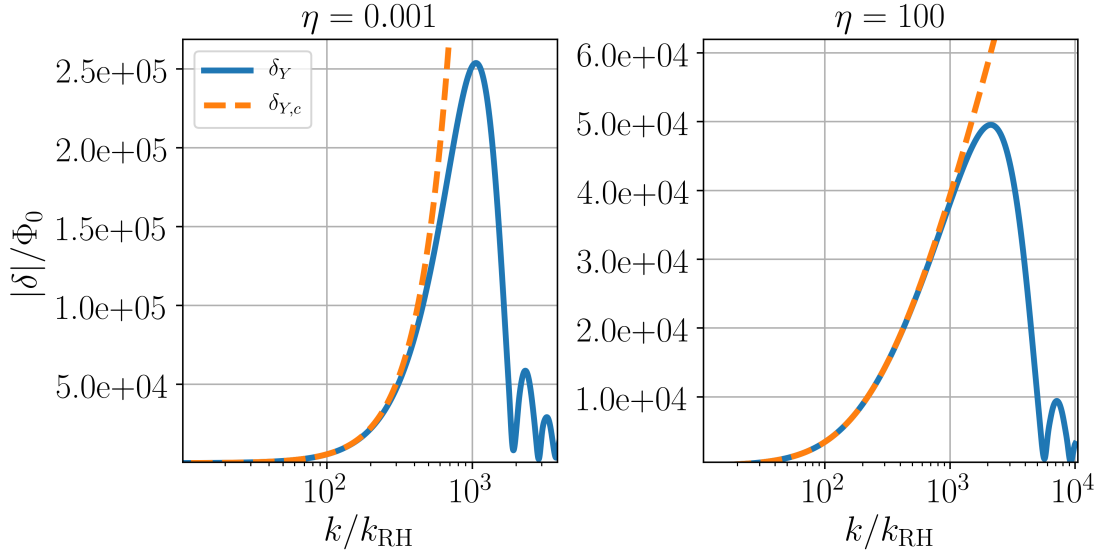
Figure 9. Comparing the amplitude of the first and second peaks in $\delta_Y(k)$. For both $\eta < 1$ and $\eta > 1$, the second peak amplitude $\lesssim 0.25 \delta_Y(k_{\rm pk})$.

5.1 Scenarios with initially subdominant Y particles

Figure 10 shows $T(k)$ for $m = 2\,\text{TeV}$, $T_{\rm RH} = 20\,\text{MeV}$ and $\eta = 500$. The transfer function equals unity for $k \lesssim k_{\rm J,min}$. As k increases beyond $k_{\rm J,min}$, $T(k)$ falls off in amplitude as δ_Y is increasingly suppressed relative to $\delta_{Y,c}$. After the fall-off, $T(k)$ shows oscillations in k that reflect the small-scale decaying oscillations of $\delta_Y(k)$ due to the pressure of the Y particles. Figure 10 also shows the transfer function used in B19, given by $\exp[-k^2/(2k_y^2)]$, and we see that our transfer function falls off at comparatively smaller k values.
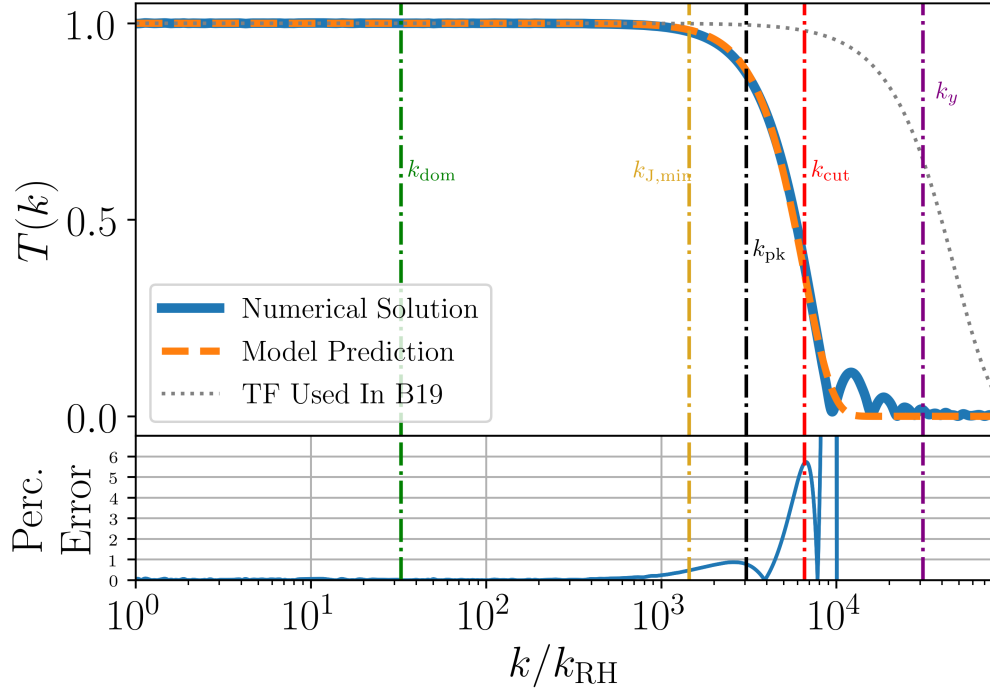
The dashed orange curve in figure 10 shows the fit to $T(k)$ using the function given by eq. (5.2), with fit parameters $k_{\rm cut}/k_{\rm RH} = 6539$ and $n = 2.7$. The bottom panel shows the percentage error between $T(k)$ and the fitting function. At $k = k_{\rm pk}$, the value of the fitting function is within 1% of the numerical value of $T(k)$.

For η between 3 and 1500, the best-fit values for n are between 2.60 and 2.78. Since this variation is small for a range of η that spans nearly two orders of magnitude, we fix $n = 2.7$ for $\eta > 1$. With n fixed, we derive an expression for the cut-off scale $k_{\rm cut}$ by relating it to the peak scale evaluated in section 4.2. For $k \geq 10 k_{\rm dom}$, the numerical solutions for $\delta_{Y,c}(k)$ follow a logarithmic function of $a_{\rm dom}/a_k$, where the mode k enters the horizon at a_k:

$$\delta_{Y,c}(k > 10 k_{\rm dom}, a_{\rm RH}) = 4.86 \Phi_0 \left(\frac{k_{\rm dom}}{k_{\rm RH}} \right)^2 \ln \left(0.21 \left[\frac{g_*(T(a_k))}{g_*(T_{\rm dom})} \right]^{\frac{1}{6}} \frac{k}{k_{\rm dom}} \right), \qquad (5.3)$$

where eq. (B.11) was used to express $a_{\rm dom}/a_k$ in terms of $k/k_{\rm dom}$. Differentiating $\delta_Y(k) = \delta_{Y,c}(k) T(k)$ with respect to k, while ignoring the weak k-dependence of $g_*(T(a_k))$ and using the expression for $T(k)$ given by eq. (5.2) with $n = 2.7$ generates a relation between $k_{\rm cut}$ and the peak wavenumber $k_{\rm pk}$ that maximizes $\delta_Y(k)$:

$$\frac{k_{\rm cut}}{k_{\rm pk}} = \left[2.7 \log \left(0.21 \left[\frac{g_*(T(a_{\rm pk}))}{g_*(T_{\rm dom})} \right]^{\frac{1}{6}} \frac{k_{\rm pk}}{k_{\rm dom}} \right) \right]^{\frac{1}{2.7}}. \qquad (5.4)$$

Figure 10. Transfer function $T(k) \equiv \delta_Y(k)/\delta_{Y,c}(k)$, evaluated at $a_{\rm RH}$ for $m = 2\,{\rm TeV}$, $T_{\rm RH} = 20\,{\rm MeV}$ and $\eta = 500$. The dashed orange curve shows $T(k)$ given by our model, with $k_{\rm cut}$ given by eq. (5.5) and $n = 2.7$. The transfer function $\exp[-k^2/(2k_y^2)]$ used in B19 is shown by the grey dotted curve, where k_y is the wavenumber corresponding to the horizon when $m = T_{\rm hs}$, given by eq. (3.8). The bottom panel shows the percentage error between $T(k)$ and our model prediction.

Using eqs. (4.6) and (4.7) and the expression for $k_{\rm pk}/k_y$ from eq. (4.9), we have

$$\frac{k_{\rm cut}}{k_y} = \frac{\alpha}{b}\sqrt{\frac{\eta}{1+\eta}}\left[\frac{g_*(T(a_y))g_*(T_{\rm dom})}{g_*^2(T(a_{\rm pk}))}\right]^{\frac{1}{6}} W^{-\frac{3}{2}}(0.77\bar{g}^{\frac{1}{9}}\eta^{\frac{2}{3}})[\ln\{0.18\bar{g}^{\frac{1}{6}}\eta W^{-\frac{3}{2}}(0.77\bar{g}^{\frac{1}{9}}\eta^{\frac{2}{3}})\}]^{0.37},$$

(5.5)

where $\bar{g} = g_*^2(T_i)/g_*(T_{\rm dom})g_*(T(a_{\rm pk}))$, W is the Lambert W-function and b is 2.70 if the Y particles are bosons and 3.15 if they are fermions. The coefficient α accounts for the slight difference in the peak scale values for Y particles following different statistics, as described in section 4.2: $\alpha = 1.82$ and 1.84 for bosonic and fermionic Y particles, respectively.

The numerical solutions for three values of η are shown in figure 11 along with the curves given by eq. (5.2) with $n = 2.7$ and $k_{\rm cut}$ calculated using eq. (5.5). The percentage errors between the functional forms and $T(k)$ are plotted in the bottom panel. For $\eta = 1500$, which was the maximum value of η for which $T(k)$ was computed, the functional form with $n = 2.7$ is within 1% of the numerical value of $T(k)$ at $k_{\rm pk}$. The percentage error remains less than 8% for $T(k) \geq 0.25$. The numerically determined $k_{\rm cut}$ is within 4% of the analytical expression given by eq. (5.5) for $\eta > 50$.

For smaller values of η, $k_{\rm cut} \lesssim 10k_{\rm dom}$, and the expression given by eq. (5.3) becomes increasingly inaccurate. In addition, our analytical prediction of $k_{\rm pk}$ diverges from the peak wavenumber in the range $\eta < 50$. Thus, the prediction of $k_{\rm cut}$ given by eq. (5.5) becomes inaccurate. For $1.1 \leq \eta \leq 50$, we empirically find that a power law describes the variation of
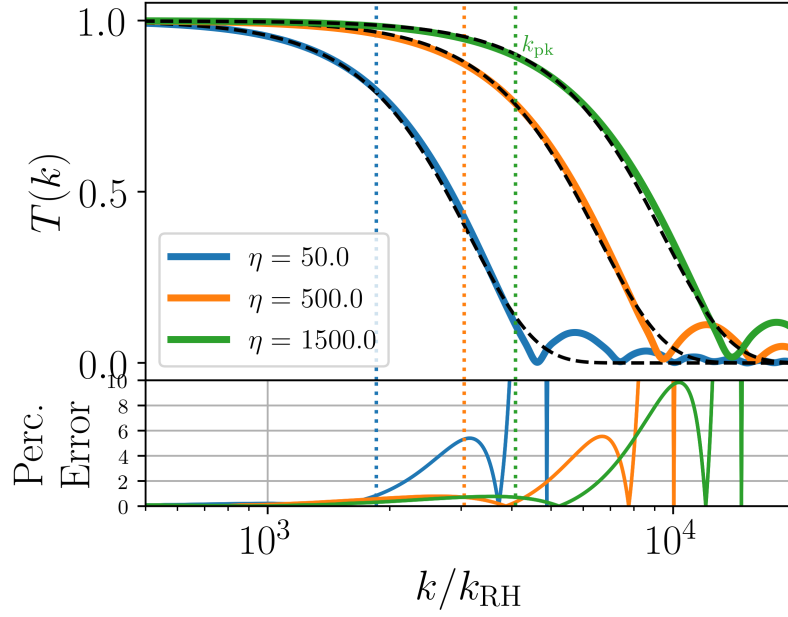
Figure 11. *Top*: the functional form $T(k) = \exp[-(k/k_{\rm cut})^{2.7}]$ (dashed black lines) compared to the numerically evaluated $T(k) = \delta_Y(k)/\delta_{Y,c}(k)$ at $a_{\rm RH}$ for three different values of η. The dotted vertical lines mark $k_{\rm pk}$. The value of $k_{\rm cut}$ is given by eq. (5.5). *Bottom*: percentage error between the numerical $T(k)$ and the best fit functions.

$k_{\rm cut}/k_y$ with η:

$$\frac{k_{\rm cut}}{k_y} = \frac{\alpha + 0.15}{b} \eta^{-0.21}. \tag{5.6}$$

This expression predicts the cut-off scale to within 2.5% error for $1.1 \le \eta \le 50$.

In the $\eta > 1$ regime in figure 12 we show the numerically determined $k_{\rm cut}$ divided by k_y as points plotted for different values of η for cases when the Y particles are bosons (red) and fermions (black). For $\eta > 50$, the expressions given by eq. (5.5) are plotted as the solid curves. For $1 < \eta < 50$, the power law fits given by eq. (5.6) are plotted as the dashed curves. The numerically determined $k_{\rm cut}/k_y$ values are shown for $m = 2\,{\rm TeV}$ (dots) and $m = 200\,{\rm GeV}$ (crosses). The overlap of the dots and crosses demonstrates that the validity of the power law fit of eq. (5.6) is independent of m.

5.2 Scenarios with initial Y-domination

If $\eta < 1$, the universe is initially dominated by the energy density of the Y particles, and $\delta_{Y,c}(k, a_{\rm RH}) \propto a_{\rm RH}/a_k \propto (k/k_{\rm RH})^2$ for all $k \gtrsim k_{\rm RH}$. From our numerical solutions, we find

$$\delta_{Y,c}(k, a_{\rm RH}) = 0.62 \Phi_{0m} \left(\frac{k}{k_{\rm RH}} \right)^2. \tag{5.7}$$

Here, $\delta_{Y,c}$ is evaluated by setting the initial conditions outlined in appendix C, and $\Phi_{0m} = 9\Phi_0/10$ is the primordial metric perturbation in a matter-dominated universe. This expression for $\delta_{Y,c}(k, a_{\rm RH})$ is used to evaluate $T(k)$ when $\eta < 1$.

We fit the functional form $\exp[-(k/k_{\rm cut})^n]$ to the transfer function, treating n and $k_{\rm cut}$ as free parameters. From fitting $T(k)$ for $10^{-3} < \eta < 1$, the η-dependence of n can be
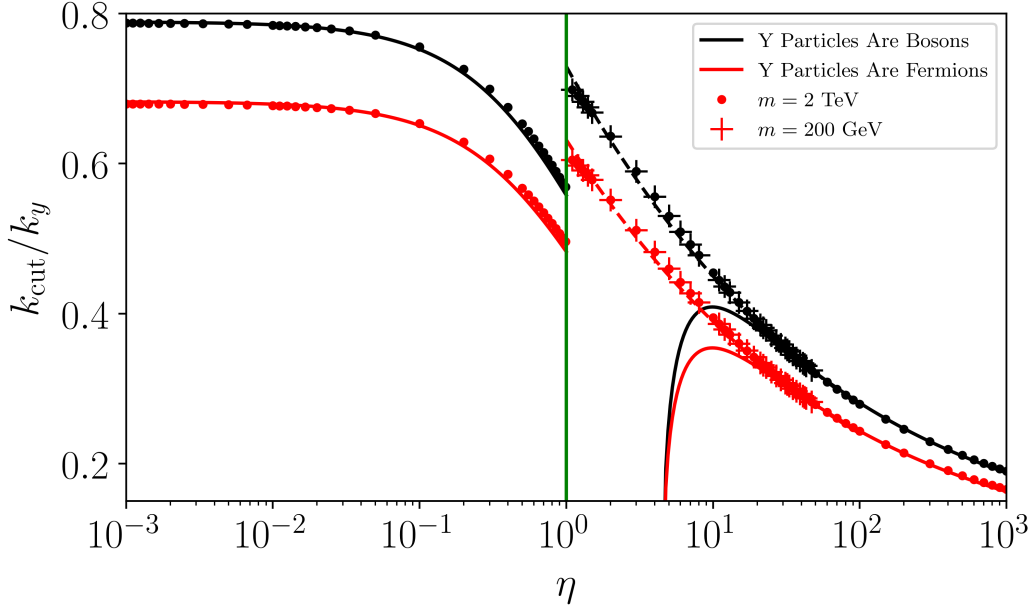
Figure 12. The cut-off scale wavenumber for the transfer function, plotted as $k_{\rm cut}/k_y$ against η, the initial value of ρ_R/ρ_Y. The different colors indicate Bose-Einstein or Fermi-Dirac statistics for the Y particles. The solid curves for $\eta > 50$ show the analytical predictions for $k_{\rm cut}/k_y$ given by eq. (5.5), whereas the dashed curves show the power law fits given by eq. (5.6) for $1 < \eta < 50$. The solid curves for $\eta < 1$ show the analytical predictions given by eq. (5.11). The dots and crosses represent the $k_{\rm cut}$ determined by fitting the functional form $\exp[-(k/k_{\rm cut})^n]$, with crosses showing cases with $m = 200\,{\rm GeV}$ and dots showing $m = 2\,{\rm TeV}$ for the range $1 < \eta < 50$. This plot assumes $g_*(T) = g_{*S}(T) = 100$.

summarized as

$$n = \begin{cases} 2.2 - 0.29(\eta - 0.1) & 0.1 \le \eta < 1 \\ 2.2 & \eta < 0.1. \end{cases} \tag{5.8}$$

The value of n falls with increasing η in the range $0.1 \le \eta < 1$ as the contribution of the SM radiation density to the Hubble rate becomes increasingly significant. To find an analytical expression for $k_{\rm cut}$, we use eq. (5.7) with $T(k) = \exp[-(k/k_{\rm cut})^n]$ and maximize $\delta_Y(k) = T(k)\delta_{Y,c}(k)$ with respect to k to obtain the peak wavenumber $k_{\rm pk}$ in terms of $k_{\rm cut}$:

$$\frac{k_{\rm cut}}{k_{\rm pk}} = \left(\frac{n}{2}\right)^{1/n}. \tag{5.9}$$

Substituting $k_{\rm pk}/k_y$ from eq. (4.13), we have

$$\frac{k_{\rm cut}}{k_y} = \frac{\gamma}{b}\left(\frac{n}{2}\right)^{\frac{1}{n}}\frac{1}{\sqrt{1+\eta}}, \tag{5.10}$$

where $\gamma = 2.055$ and 2.065 for bosonic and fermionic Y particles, respectively, and once again, $b = 2.70$ if the Y particles are bosons and $b = 3.15$ if they are fermions.

For $\eta < 0.1$, $n = 2.2$, which can be substituted in eq. (5.10) to obtain $k_{\rm cut}/k_y = 1.04\gamma/(b\sqrt{1+\eta})$. As η increases from 0.1 to 1, n decreases linearly and $k_{\rm pk}/k_y$ increases
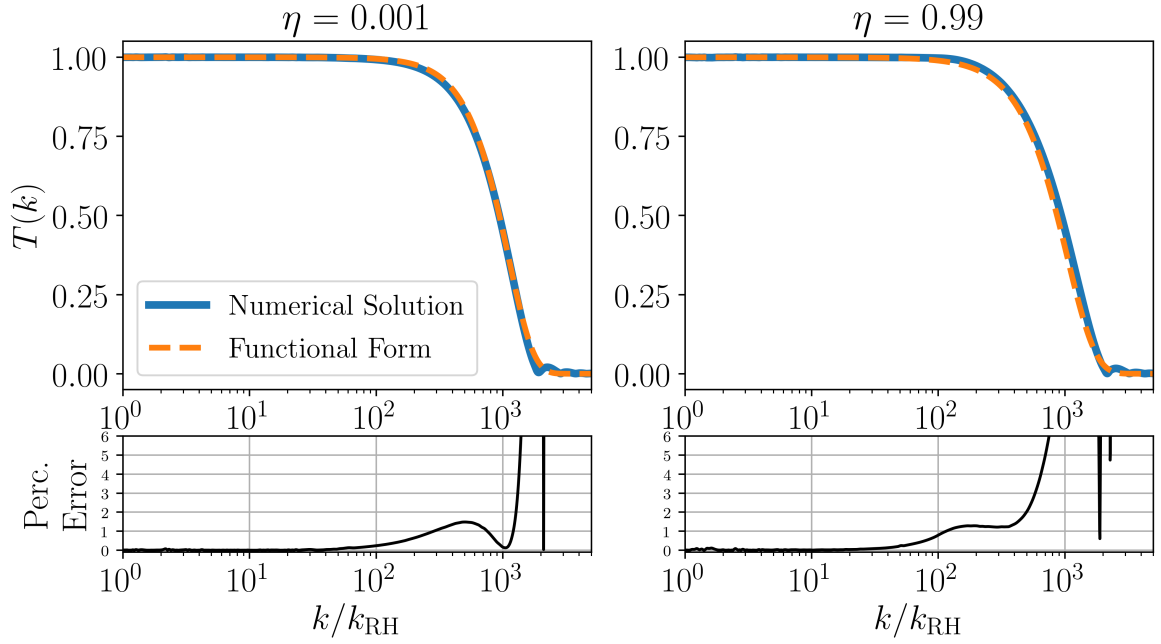
Figure 13. *Top*: numerically obtained transfer functions $T(k)$ (solid blue lines) and curves given by $\exp[-(k/k_{\rm cut})^n]$ (dashed orange lines) for the cases $\eta = 0.001$ (left) and $\eta = 0.99$ (right). For the dashed curves, $k_{\rm cut}$ is given by eq. (5.11) and n by eq. (5.8). *Bottom*: percentage error between the numerical $T(k)$ and the curves given by our models.

relative to the prediction of eq. (4.13). Since the cut-off scale follows the relation $k_{\rm cut} \propto k_{\rm pk}(n/2)^{1/n}$, the rise of $k_{\rm pk}/k_y$ nearly cancels out the effect of n decreasing. As a result,

$$\frac{k_{\rm cut}}{k_y} = \frac{1.04\gamma}{b} \frac{1}{\sqrt{1+\eta}}. \tag{5.11}$$

predicts $k_{\rm cut}$ to within 2% error even for $0.1 < \eta < 1$.

Figure 12 shows $k_{\rm cut}/k_y$ in the range $\eta < 1$ for the cases when the Y particles are bosons (red) and fermions (black). The solid lines for $\eta < 1$ show the predictions of eq. (5.11). The discontinuity at $\eta = 1$ between the analytical predictions given by eqs. (5.6) and (5.11) arises because eq. (5.7) for $\delta_{Y,c}(k)$ was used to evaluate $T(k)$ for cases with $\eta < 1$. Unlike the $\delta_{Y,c}$ used in $T(k)$ for $\eta > 1$, eq. (5.7) neglects the contribution of the SM radiation density to the Hubble rate.

Figure 13 shows $T(k)$ and the functional form $\exp[-(k/k_{\rm cut})^n]$ with $k_{\rm cut}$ given by eq. (5.11) and n by eq. (5.8), for the cases $\eta = 0.001$ (left panel) and $\eta = 0.99$ (right panel). The bottom panels show the percentage error between $T(k)$ and the functional forms.

6 The peak amplitude and observational prospects

Having determined the transfer functions and the cut-off scale, we can estimate how the EMDE impacts the dark matter annihilation rate today. Following the same procedure as ref. [34], we use the Press-Schechter formalism [45] to obtain the abundance of microhalos, and then we calculate the annihilation rate per volume assuming that the microhalos have an
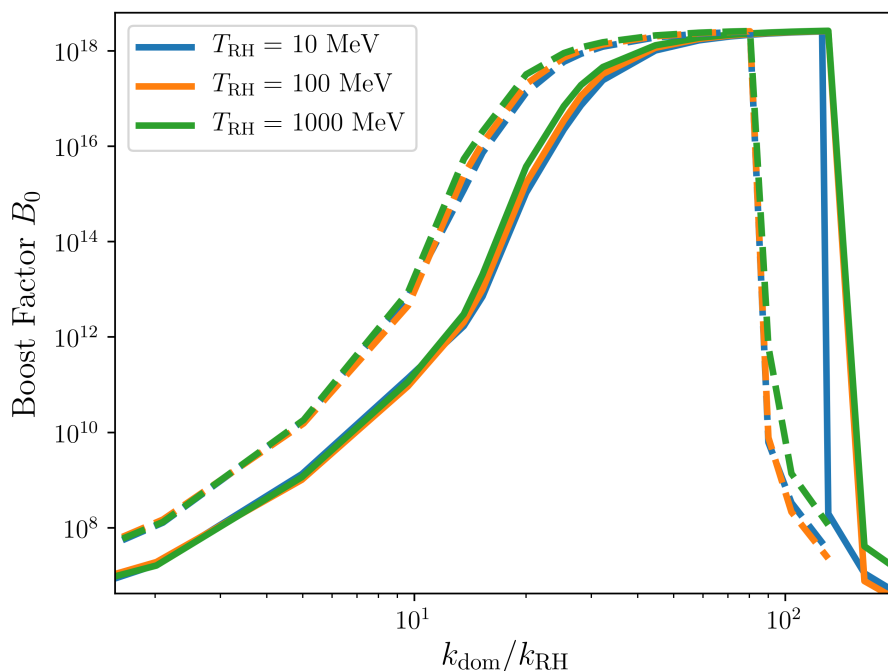
Figure 14. The boost to the DM annihilation signal as a function of the duration of the EMDE, quantified by $k_{\rm dom}/k_{\rm RH}$. The solid lines show the boost if the transfer functions given by this work are used, while the dashed lines show the boost if the transfer functions from ref. [34] are used. Using our transfer functions increases the value of $k_{\rm dom}/k_{\rm RH}$ that produces a given value of B_0 because our transfer functions suppress perturbations on larger scales, so a longer EMDE is required to generate the same enhancement to the matter power spectrum.

NFW profile with concentration $c = 2$ at their formation time. The increase of the annihilation rate due to microhalo formation is quantified by the boost factor $B(z) \equiv \langle \rho_X^2 \rangle / \langle \rho_X \rangle^2 - 1$. The resulting boost factor initially increases with time as more halos form, but then it starts to decrease as the earliest-forming microhalos are absorbed into larger halos and their Press-Schechter abundance decreases. The first microhalos are very dense and are expected to survive their absorption into larger halos [46–48], so we take the maximum value of $B(z)$ to be the boost factor today (B_0).

Figure 14 shows B_0 as a function of $k_{\rm dom}/k_{\rm RH}$ for $\eta = 12.69$, which corresponds to a hidden sector containing vector Y particles ($g = 3$) and Dirac fermion X particles ($g_X = 4$) that kinetically decoupled from the SM particles while the Y and X particles were relativistic. The solid lines show B_0 calculated using the transfer functions given by this work for three $T_{\rm RH}$ values, while the dashed lines show B_0 for the same reheat temperatures calculated using the $\exp[-k^2/(2k_y^2)]$ transfer function assumed in ref. [34]. As the duration of the EMDE increases, earlier structure formation leads to higher boost factors. The growth of density perturbations during the EMDE can even lead to halo formation prior to matter-radiation equality. Following ref. [34], we only consider halos that form at redshifts less than 10^6, and this restriction is responsible for the plateau at $B_0 \simeq 2 \times 10^{18}$. The boost increases with increasing $T_{\rm RH}$ at fixed $k_{\rm dom}/k_{\rm RH}$ due to a longer period of logarithmic growth for δ_X after the EMDE.

If the EMDE is long enough, microhalos form before reheating. These microhalos are dominated by Y particles, so they dissipate when the Y particles decay [34]. The released

dark matter particles have randomly oriented velocities with magnitudes boosted by nonlinear structure formation. This gravitational heating imposes a free-streaming cut-off on the power spectrum after reheating that reduces the boost factor to the standard ΛCDM prediction, $B_0 \sim 10^6$. We implement gravitational heating following the "optimistic" approach from ref. [34]: a free-streaming cut-off is applied to the matter power spectrum based on the minimum virial velocity of the halos that contain 20% of the dark matter at the end of the EMDE, and no free-streaming cut-off is imposed if less than 20% of the dark matter is bound into halos during the EMDE. The sharp decrease in B_0 due to gravitational heating can be seen at $k_{\mathrm{dom}}/k_{\mathrm{RH}} \simeq 100$ in figure 14. The slight red tilt of the primordial power spectrum causes the reduction of the boost due to gravitational heating to move to higher values of $k_{\mathrm{dom}}/k_{\mathrm{RH}}$ for higher T_{RH}.

Figure 14 shows that B_0 for $k_{\mathrm{dom}}/k_{\mathrm{RH}} \lesssim 80$ is smaller for our transfer functions compared to those from ref. [34]; our transfer functions suppress longer-wavelength perturbations, which reduces the amplitude of the peak in the power spectrum and delays the formation of bound structures. For $k_{\mathrm{dom}}/k_{\mathrm{RH}} \gtrsim 80$, the comparatively fewer microhalos predicted by our transfer functions at reheating implies that the reduction of the boost due to gravitational heating happens for larger $k_{\mathrm{dom}}/k_{\mathrm{RH}}$ (longer EMDEs) compared to when the transfer functions from ref. [34] are used.

Figure 14 demonstrates that the annihilation boost does not strongly depend on T_{RH}, but it is highly sensitive the duration of the EMDE, which sets the peak amplitude of the matter power spectrum for a fixed value of η. While the peak scale controls the size of the first microhalos that form during or after an EMDE, the peak amplitude determines their formation times because gravitational collapse occurs when $\delta \simeq 1.68$. The central density of a halo forming at a_f scales as a_f^{-3}. Consequently, structures form earlier and have denser cores if the power spectrum has a higher peak [42], which yields larger annihilation boosts up to the point that the peak becomes high enough that halos form during the EMDE.

If the Y particles initially dominate the universe, the amplitude of the peak in the matter power spectrum depends only on the duration of EMDE: a longer EMDE implies a longer period of linear perturbation growth, translating to a higher peak in the power spectrum. If the Y particles are initially subdominant, then the peak amplitude also depends on how long the universe remains radiation dominated after the Y particles become nonrelativistic. Figure 15 demonstrates that a_{dom}/a_p depends exclusively on η: a_{dom}/a_p remains the same if m is varied while η is held fixed. We use the transfer functions derived in the previous section to calculate $\delta_{\mathrm{pk}} \equiv \delta_Y(k_{\mathrm{pk}})$ and evaluate observational prospects in terms of η and the duration of the EMDE.

If the Y particle is initially subdominant ($\eta > 1$), the following fitting function describes $\delta_{Y,c}(k, a_{\mathrm{RH}})$ well for $k > 10k_{\mathrm{RH}}$:

$$\delta_{Y,c}(k > 10k_{\mathrm{RH}}, a_{\mathrm{RH}}) = 0.596\Phi_0 \left(\frac{k_{\mathrm{dom}}}{k_{\mathrm{RH}}}\right)^2 \frac{\ln(1 + 0.22q)}{0.22q} q^2 p(q), \tag{6.1}$$

where $q = k/k_{\mathrm{dom}}$ and $p(q) = [1 + 1.11q + (0.94q)^2 + (0.63q)^3 + (0.45q)^4]^{-1/4}$. The peak amplitude is $\delta_Y(k_{\mathrm{pk}}) = \delta_{Y,c}(k_{\mathrm{pk}})T(k_{\mathrm{pk}})$, where $T(k) = \exp[-(k/k_{\mathrm{cut}})^{2.7}]$. Equation (6.1) shows that $\delta_{Y,c}(k_{\mathrm{pk}})$ is separable into $(k_{\mathrm{dom}}/k_{\mathrm{RH}})^2$, which sets the duration of the EMDE, times a function of $k_{\mathrm{pk}}/k_{\mathrm{dom}}$. The ratio $k_{\mathrm{pk}}/k_{\mathrm{dom}}$ depends only on η and the Y particle statistics, as shown by eq. (4.6). Furthermore, $k_{\mathrm{pk}}/k_{\mathrm{cut}}$ also depends only on η and the statistics of the Y particles, as illustrated by eqs. (5.5) and (5.6). The peak scale is given by eq. (4.9), and eq. (5.5) provides k_{cut} for $\eta > 50$. For $1 < \eta < 50$, the power-law fit of eq. (5.6)
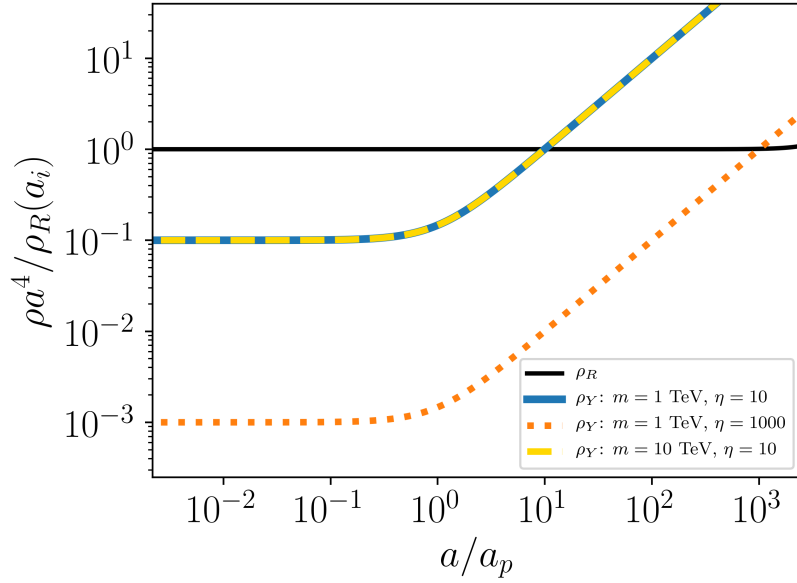
Figure 15. The effect of varying m and η on the evolution of SM and Y densities. The solid blue, dashed yellow and dotted orange lines show $\rho_Y a^4$ as a function of a/a_p, where a_p is the scale factor at which the Y particles can be considered to have become nonrelativistic. The EMDE begins when the respective lines cross the horizontal black line, which shows $\rho_R a^4$. The blue and orange lines have the same $m = 1\,\mathrm{TeV}$ but different η; a_{dom}/a_p differs for these cases. In contrast, the solid blue and dashed yellow lines have the same a_{dom}/a_p even with different values of m since η is the same.

gives k_{cut}, and the peak scale is well-described by the fit

$$\frac{k_{\mathrm{pk}}}{k_y} = \frac{\alpha - 0.18}{b}\eta^{-0.299}, \tag{6.2}$$

where $\alpha = 1.82$ and $b = 2.70$ for bosonic Y particles and $\alpha = 1.84$ and $b = 3.15$ for fermionic Y particles. This prescription for calculating δ_{pk} matches the numerically determined maximum of $\delta_Y(k)$ to within 4%. As expected, $\delta_{\mathrm{pk}} \equiv \delta_Y(k_{\mathrm{pk}})$ depends on $k_{\mathrm{dom}}/k_{\mathrm{RH}}$ and η.

Figure 16 shows $\delta_{\mathrm{pk}}/\delta_Y(k_{\mathrm{RH}})$ at a_{RH} for a bosonic Y particle, where $\delta_Y(k_{\mathrm{RH}}, a_{\mathrm{RH}}) \simeq 3.05\Phi_0$ is the value of δ_Y at the scale at which the power spectrum begins deviating from the power spectrum in scenarios without an EMDE, and we have continued to neglect the scale-dependence of Φ_0. Since $\delta_Y(k) \simeq \delta_X(k)$, and $\delta_X(k)$ only logarithmically increases with k for modes that enter the horizon during radiation domination, this ratio nearly equals the maximum enhancement to the power spectrum. Figure 16 shows that δ_{pk} increases with increasing $k_{\mathrm{dom}}/k_{\mathrm{RH}}$, as expected. Figure 16 also shows that δ_{pk} is rather sensitive to η for $\eta \lesssim 10$, but that sensitivity wanes as η increases. As can be seen in figure 4, $\delta_Y(k)$ continues to rise steeply with k for $k \gtrsim k_{\mathrm{dom}}$ and plateaus when $k \gtrsim 10k_{\mathrm{dom}}$. Therefore, δ_{pk} sharply depends on k_{pk} if $k_{\mathrm{pk}} \lesssim 10k_{\mathrm{dom}}$ but then becomes less sensitive to k_{pk} as increasing η increases $k_{\mathrm{pk}}/k_{\mathrm{dom}}$. The variation of the peak height with η thus becomes weaker, as indicated by the contours in figure 16 becoming increasingly vertical as η increases.

If the Y particles dominate the universe before they become nonrelativistic ($\eta < 1$), the expression for $\delta_{Y,c}$ from eq. (5.7) implies that

$$\delta_{\mathrm{pk}} = 0.62\Phi_{0m}\left(\frac{k_y}{k_{\mathrm{RH}}}\right)^2\left(\frac{k_{\mathrm{pk}}}{k_y}\right)^2 \exp\left[-\left(\frac{k_{\mathrm{pk}}}{k_{\mathrm{cut}}}\right)^n\right], \tag{6.3}$$
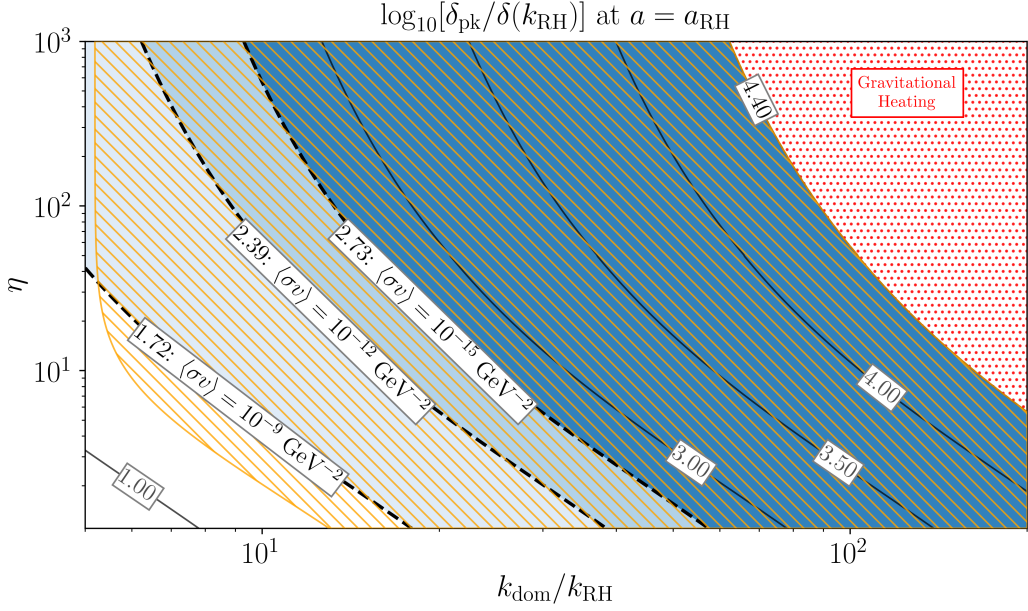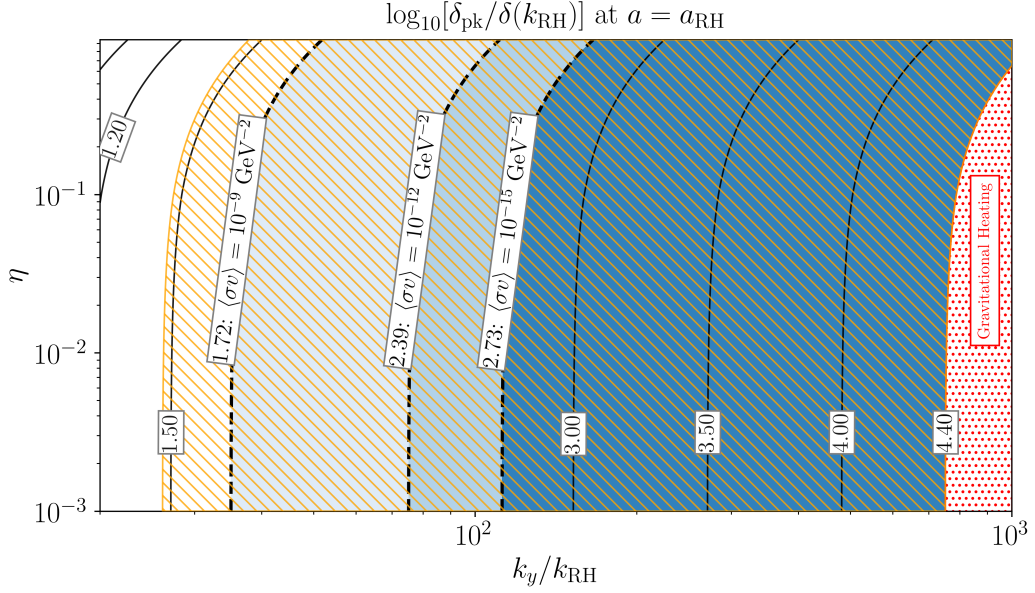
Figure 16. Contours of $\log_{10}[\delta_{\rm pk}/\delta(k_{\rm RH})]$, the maximum enhancement to δ_Y at the end of the EMDE, as a function of η and $k_{\rm dom}/k_{\rm RH}$ for cases in which the universe is initially dominated by SM radiation. This plot takes $g_*(T) = 100$. The red dotted region shows cases in which microhalos are erased at the end of the EMDE and gravitational heating suppresses structure formation after the EMDE. The thick dashed contours mark the largest $k_{\rm dom}/k_{\rm RH}$ values that are compatible with IGRB observations for three values of the DM annihilation cross-section and $m_X = 10^6$ GeV, with the labels showing the $\langle\sigma v\rangle$ value considered. For instance, the white region to the left of the dashed contour with $\log_{10}[\delta_{\rm pk}/\delta(k_{\rm RH})] = 1.72$ is allowed for $\langle\sigma v\rangle \geq 10^{-9}$ GeV^{-2}. The deep blue region is excluded if $\langle\sigma v\rangle \geq 10^{-15}$ GeV^{-2}. The yellow hatched region can be probed with pulsar timing arrays with 100 pulsars observed weekly for 25 years for cases with $T_{\rm RH} \lesssim 20$ MeV.

where $k_{\rm pk}/k_{\rm RH}$ was split into $(k_y/k_{\rm RH})(k_{\rm pk}/k_y)$. The expressions for $k_{\rm pk}/k_y$ and $k_{\rm cut}/k_y$ can be taken from eqs. (4.13) and (5.11) respectively, while n is given by eq. (5.8). The peak amplitude can be predicted to within 4% error for $\eta < 1$ using these expressions.

Equation (6.3) shows that $\delta_{\rm pk}$ is proportional to $(k_y/k_{\rm RH})^2$; this ratio sets the duration of the EMDE. Apart from $k_y/k_{\rm RH}$, the other factors in eq. (6.3) depend only on η and the Y particle statistics. For $\eta < 0.1$, the η-dependence becomes negligible as the universe becomes increasingly Y-dominated at the time of horizon entry of the peak scale. Figure 17 shows the peak enhancement to δ_Y at the end of the EMDE as a function of $k_y/k_{\rm RH}$ and η for a bosonic Y particle. The contours show that $\delta_{\rm pk}$ increases with $k_y/k_{\rm RH}$ as the EMDE becomes longer and that the enhancement is independent of η for $\eta < 0.1$.

For very long EMDEs, B_0 falls below 10^8 due to gravitational heating (as can be seen in figure 14). All scenarios with higher power spectrum peaks will be similarly affected by the destruction of bound structures during reheating. In figures 16 and 17, the red dotted regions indicate points with $\delta_{\rm pk}/\delta(k_{\rm RH}) \gtrsim 10^{4.4}$, which is the peak enhancement for $\{\eta, k_{\rm dom}/k_{\rm RH}\} = \{12.69, 150\}$. These areas mark the parameter combinations for which gravitational heating reduces the abundance of microhalos after the EMDE.

If dark matter is a thermal relic, then it is possible to constrain EMDE cosmologies using limits on the dark matter annihilation rate. Reference [34] calculated an annihilation

$$\log_{10}[\delta_{\rm pk}/\delta(k_{\rm RH})] \text{ at } a = a_{\rm RH}$$

Figure 17. Contours of $\log_{10}[\delta_{\rm pk}/\delta(k_{\rm RH})]$, the maximum enhancement to δ_Y at the end of the EMDE, as a function of η and $k_y/k_{\rm RH}$ for cases in which the universe is initially dominated by the Y particles. The red dotted region shows cases in which microhalos form during the EMDE and gravitational heating suppresses structure formation after the EMDE. The thick dashed contours show the limits of the parameter space compatible with IGRB observations for three values of the DM annihilation cross-section and $m_X = 10^6$ GeV, with the labels showing the $\langle\sigma v\rangle$ value considered. The yellow hatched region can be probed with pulsar timing arrays with 100 pulsars observed weekly for 25 years for cases with $T_{\rm RH} \lesssim 20$ MeV.

rate per mass in a given volume if the dark matter resides within a population of microhalos:

$$\frac{\Gamma_{\rm DM}}{M_X} = \frac{1}{2}\left(\frac{\langle\sigma v\rangle/m_X^2}{\rm GeV^{-4}}\right) B_0 \times (8.098 \times 10^{-47}) \times \Omega_X h^2, \tag{6.4}$$

where $\langle\sigma v\rangle$ is the velocity-averaged DM annihilation cross-section and M_X is the total dark matter mass in the volume. Since the annihilation rate in these scenarios is proportional to the number density of microhalos and thus the dark matter density, the annihilation signal produced is similar to that from decaying dark matter. Assuming that annihilation and decay events both produce two primary particles, the annihilation rate can be related to an effective DM lifetime by equating the rate of particle production from annihilation, $2M_X(\Gamma_{\rm DM}/M_X)$, to the particle production rate from decaying DM of mass $2m_X$ and lifetime τ, given by $(2/\tau)[M_X/(2m_X)]$. This yields $\tau_{\rm eff}^{-1} = 2m_X(\Gamma_{\rm DM}/M_X)$, which should be compared to the bounds on the lifetime of DM particles with mass $2m_X$.

Using Fermi-LAT observations of the Isotropic Gamma Ray Background (IGRB) [49], ref. [50] established $\tau_{\rm eff} \gtrsim 10^{28}$ seconds for a variety of decay channels and DM masses ranging from 10 GeV to 10^9 GeV. By connecting B_0 to peak height, we can estimate the allowed regions of the EMDE parameter space based on this lower limit on $\tau_{\rm eff}$. Using $\Omega_X h^2 = 0.12$ and $m_X = 10^6$ GeV, the IGRB constraint on $\tau_{\rm eff}$ translates to $B_0 \lesssim 10^{10}$ for $\langle\sigma v\rangle = 10^{-9}$ GeV^{-2}, which is close to the canonical WIMP DM cross-section of 2.2×10^{-26} cm^3 s^{-1} [51]. From figure 14, we see that $\{\eta, k_{\rm dom}/k_{\rm RH}\} = \{12.69, 7\}$ corresponds to $B_0 = 10^{10}$. The white unshaded region to the bottom left in figure 16 marks all points with

$\delta_{\rm pk}$ values that are smaller than $\delta_{\rm pk}$ for $\{\eta, k_{\rm dom}/k_{\rm RH}\} = \{12.69, 7\}$, marking the allowed parameter space based on this constraint. The white unshaded region to the left in figure 17 marks the allowed area of the η-$k_y/k_{\rm RH}$ space for cases with $\eta < 1$ based on the same peak height limits.

If the DM particle freezes out during or before the EMDE, then a smaller annihilation cross section is required to generate the observed DM density [22, 52, 53]. Lowering the cross-section increases the upper limit on B_0, expanding the allowed parameter space. Considering $\langle \sigma v \rangle = 10^{-12} \ {\rm GeV}^{-2}$, the light blue regions to the left of the thick dashed contour line with $\log_{10}[\delta_{\rm pk}/\delta(k_{\rm RH})] = 2.39$ are allowed in addition to the white regions in figures 16 and 17. With $\langle \sigma v \rangle = 10^{-15} \ {\rm GeV}^{-2}$, the allowed region increases to include the medium blue regions to the left of the contour lines with $\log_{10}[\delta_{\rm pk}/\delta(k_{\rm RH})] = 2.73$, with only the deep blue regions excluded in both plots.

The annihilation contours in figures 16 and 17 are presented as estimates because they assume that the relation between B_0 and $\delta_{\rm pk}$ for a single value of η can be extended to other η values. Power spectra with the same peak heights have different peak scales for different values of η, but the fact that B_0 is largely insensitive to $T_{\rm RH}$ indicates that B_0 does not depend strongly on $k_{\rm pk}$. Changing η also changes the shape of the power spectrum around its peak. The impact of peak shape on B_0 has not been extensively studied, but the values for B_0 computed in ref. [35] for a power spectrum with $\eta \ll 1$ and the B_0 values for $\eta = 12.69$ in figure 14 differ by less than an order of magnitude for power spectra with the same $\delta_{\rm pk}$. We conclude that the $B_0 - \delta_{\rm pk}$ relation for $\eta = 12.69$ provides a strong indication of which $\delta_{\rm pk}$ values can be ruled out by limits on the dark matter annihilation rate.

It is also possible to detect the microhalos that form after an EMDE through their gravitational influence. Pulsar timing arrays (PTAs) are promising probes of EMDE cosmologies [54, 55]: PTAs are sensitive to both the Shapiro time delays as signals pass through microhalos and the Doppler shifts that result when a microhalo pulls on a pulsar, with the latter being most sensitive to sub-earth-mass microhalos [56]. With weekly observations and an RMS timing residual of 10 ns, ref. [55] showed that microhalos resulting from EMDE-enhanced power spectra with $T_{\rm RH} \lesssim 20 \ {\rm MeV}$ and $k_{\rm cut}/k_{\rm RH} > 20$ can be detected at 2σ significance if 100 pulsars are observed for 25 years or if 1000 pulsars are observed for 15 years.

Reference [55] used power spectra from initially Y-dominated EMDEs [29] with a Gaussian cut-off. A cut-off given by $k_{\rm cut}/k_{\rm RH} = 20$ on their power spectra implies that $\delta(k)$ peaks at around $24k_{\rm RH}$ with a value close to $27\delta(k_{\rm RH})$. Consequently, power spectra with $\delta(24k_{\rm RH}) \gtrsim 27\delta(k_{\rm RH})$ will produce microhalos that have similar detection prospects to those produced by initially Y-dominated EMDE scenarios with $k_{\rm cut}/k_{\rm RH} \gtrsim 20$. Such cases are marked by the yellow hatched regions in figures 16 and 17; we expect that these EMDE scenarios with $T_{\rm RH} \lesssim 20 \ {\rm MeV}$ will generate signals that are detectable by the PTAs described above.

Another possible method of observing the microhalos resulting from an EMDE comes from how they impact the magnification of stars that pass behind the lensing caustics of galaxy clusters [57–59]. As the star passes through the caustic, fluctuations in the dark matter density generate variations in the star's brightness, which can be used to detect sub-earth-mass microhalos. Reference [42] identified the ranges of microhalo masses and central densities that can be detected using this method by imposing lower bounds on the magnitude of the observed brightness fluctuations and on the abundance of microhalos. They demonstrated that microhalos that meet their detection criteria are generated by a power

spectrum that rises as k^4 for $k_{\rm RH} < k < k_{\rm pk}$ and decreases sharply for $k > k_{\rm pk}$, reaching a peak enhancement of 10^4 times the ΛCDM power spectrum at $k_{\rm pk} \approx 10^{8.5} k_{\rm eq}$, where $k_{\rm eq}$ is the horizon scale at matter-radiation equality. Employing our transfer functions, the parameters $T_{\rm RH} = 4\,{\rm MeV}$ with $\eta = 0.01$ and $k_y/k_{\rm RH} = 100$ generate a power spectrum with a k^4 rise before a peak at the scale $k_{\rm pk} \approx 10^{8.5} k_{\rm eq}$. The peak enhancement is $\delta_{\rm pk}/\delta(k_{\rm RH}) = 126$, corresponding to a power spectrum peak enhancement factor of $\approx 10^4$. Using $T_{\rm RH} = 4\,{\rm MeV}$, $\eta = 8$ and $k_{\rm dom}/k_{\rm RH} = 20$ generates a power spectrum with a similar peak scale and peak enhancement. Although the scaling is not strictly k^4 for $k_{\rm RH} < k < k_{\rm pk}$ in this case, the power spectrum is logarithmic for only a narrow range of k near the peak, making this power spectrum roughly similar to one that rises as k^4 before the peak. For similar peak enhancements, power spectra with a k^4 rise before the peak and larger $k_{\rm pk}$ values from cases with $T_{\rm RH}$ up to a few hundred MeV also result in microhalos that can be detected using caustic microlensing observations [42].

7   Summary and discussion

The linear growth of dark matter perturbations during an early matter-dominated era (EMDE) leads to the formation of microhalos much earlier than in standard cosmologies [29, 30, 32]. These dense microhalos may be detected gravitationally by upcoming pulsar timing arrays [42, 54, 55] and through their impact on stellar microlensing events in galaxy clusters [42, 57–59]. They can also boost the dark matter annihilation rate by several orders of magnitude [32, 34, 35]. Perturbation growth is suppressed for modes that enter the horizon while the particle that dominates the universe during the EMDE has significant relativistic pressure. The DM power spectrum manifests this suppression as a small-scale cut-off, which strongly affects the DM annihilation signal [32, 35]. The small-scale cut-off also impacts the prospects of detecting the structures formed in EMDE cosmologies via pulsar timing arrays [42, 54, 55] and caustic microlensing [42]. It is therefore important to accurately calculate this cut-off scale, so that EMDE scenarios with initially hot hidden sectors may be tested against observational data. In this paper, we have investigated the small-scale cut-off in the matter power spectrum that results from the relativistic initial state of the particle responsible for the EMDE.

   We employed a custom Boltzmann solver to calculate the evolution of perturbations in a universe with an initially relativistic hidden sector particle (Y). We found that the evolution of subhorizon perturbations in the Y particle density (δ_Y) depends on the wavelength of the perturbation mode compared to a time-varying Jeans length. This Jeans length is set by the sound speed of the Y particles, and it increases while they are relativistic and then starts decreasing after they transition to nonrelativistic behavior. As long as the Jeans length is greater than a perturbation mode's wavelength, δ_Y oscillates, while it grows when the Jeans length drops below the mode wavelength. Therefore, linear growth during the EMDE starts later for smaller-scale modes. This suppression of growth due to relativistic pressure generates a peak in the power spectrum of δ_Y: for wavelengths smaller than the peak scale, the power spectrum falls off in amplitude due to the delayed onset of growth during the EMDE, whereas longer wavelength modes have less time to grow during the EMDE because they enter the horizon later. This peak is inherited by the dark matter power spectrum as dark matter particles fall into the gravitational wells created by the clustered Y particles during the EMDE.

To describe how the relativistic pressure of the Y particles affects the matter power spectrum, we provided transfer functions that relate the matter perturbations of initially cold and hot hidden sectors. These transfer functions generate the matter power spectrum following an EMDE arising from an initially hot hidden sector without the cumbersome calculation of the density evolution of the hidden sector particle as it transitions from relativistic to nonrelativistic behavior. The transfer functions take the form $\exp[-(k/k_{\rm cut})^n]$, where n depends on $\rho_{\rm SM}/\rho_Y$ when the Y particles were relativistic (η) and $k_{\rm cut}$ is the cut-off scale. We found that $k_{\rm cut}/k_y$ is a function of η and the Y particle statistics, where k_y is the wavenumber of the mode that enters the horizon when the hidden sector temperature equals the Y particle mass m. The ratio $k_y/k_{\rm RH}$, where $k_{\rm RH}$ is defined as the horizon wavenumber at the end of the EMDE, depends on η and is proportional to $(m/T_{\rm RH})^{2/3}$. We found that $k_{\rm cut}$ is smaller than k_y, which was used as an estimate of the cut-off scale in ref. [34]. Our result also disproves the claim in ref. [21] that the horizon scale at the start of the EMDE sets the cut-off scale.

The cut-off scale determines the power spectrum peak height, which sets the formation times and central densities of the first microhalos. The peak height $\delta_{\rm pk}$ depends on the EMDE duration and η. Longer EMDEs translate to larger $\delta_{\rm pk}$ since they involve longer periods of linear perturbation growth. For $\eta < 1$, $\delta_{\rm pk} \propto (k_y/k_{\rm RH})^2$. For $\eta > 1$, $\delta_{\rm pk} \propto (k_{\rm dom}/k_{\rm RH})^2$, where $k_{\rm dom}$ is the horizon wavenumber at the start of the EMDE. If $\eta < 0.1$, the peak height is independent of η because the subdominant SM radiation density does not affect the evolution of perturbations prior to the end of the EMDE. For $\eta > 1$, the peak height depends on η because η determines how long it takes the Y particle to dominate the universe after it becomes nonrelativistic. Relating the peak height to η and the EMDE duration enables the discussion of observational prospects and constraints in the parameter space of hidden-sector EMDE histories.

If the peak is high enough for microhalos to form during the EMDE, the evaporation of these microhalos at reheating causes the ejection of DM particles at high speeds in random directions. This gravitational heating leads to a free-streaming cut-off on the power spectrum after the EMDE. The exact evolution of this free-streaming cut-off and its relation to the abundance of microhalos that formed during the EMDE is unknown, with recent studies [60] even suggesting that the remnants of evaporated halos may re-collapse into bound structures around the epoch of matter-radiation equality. We identified the regions of parameter space where 20% or more of the dark matter is gravitationally heated; the affected parameter space has peak enhancement $\delta_{\rm pk}/\delta(k_{\rm RH}) \gtrsim 10^{4.4}$. This corresponds roughly to cases with $\eta^{1/4}k_{\rm dom}/k_{\rm RH} \gtrsim 250$ for $1 < \eta \lesssim 1000$ and $k_y/k_{\rm RH} \gtrsim 800$ for $\eta < 1$.

Since the microhalos that form after an EMDE track the dark matter density, the annihilation rate within microhalos can be compared to the rate of particle production from decaying dark matter to define an effective DM lifetime. We used constraints on the dark matter lifetime [50] based on the Fermi-LAT observations of the Isotropic Gamma Ray Background (IGRB) [49] to derive bounds on the dark matter annihilation boost B_0. By connecting the bounds on B_0 to the peak height, we identified the allowed regions of the parameter space of hidden-sector EMDE histories. Assuming a DM mass of 10^6 GeV with an annihilation cross-section close to the canonical value of 10^{-9} GeV^{-2}, the IGRB constraint allows cases obeying $\eta^{1/3}k_{\rm dom}/k_{\rm RH} \lesssim 25$ for $\eta > 1$, or cases with $k_y/k_{\rm RH} \lesssim 35$ for $\eta < 1$. Smaller cross-sections are required to match the currently observed DM relic abundance if the DM freezes out during or before an EMDE; the allowed parameter space expands for these lower cross-section values and for higher values of DM mass. Since $k_{\rm cut} < k_y$, our transfer functions

yield less structure formation for the same EMDE duration compared to ref. [34]. For cases not involving gravitational heating, we therefore obtain smaller annihilation boost factors for the same EMDE duration. In addition, this reduced structure formation also delays the onset of gravitational heating, which happens for longer EMDEs compared to ref. [34].

We also found that a large portion of the parameter space of hidden-sector EMDEs can be probed with the pulsar timing arrays discussed in ref. [55]. For example, weekly observations of 100 pulsars for 25 years would detect microhalos generated from EMDEs with $T_{\rm RH} \lesssim 20\,{\rm MeV}$, $30 \lesssim k_y/k_{\rm RH} \lesssim 800$, and $\eta < 0.1$, where the upper limit on $k_y/k_{\rm RH}$ comes from the uncertainty associated with the disruption to the post-EMDE power spectrum due to gravitational heating. If $\eta > 1$, the same PTA observations would detect microhalos resulting from EMDEs with $13 \lesssim \eta^{1/4}k_{\rm dom}/k_{\rm RH} \lesssim 250$ and $T_{\rm RH} \lesssim 20\,{\rm MeV}$. Furthermore, EMDE power spectra for reheat temperatures less than $\mathcal{O}(100\,{\rm MeV})$ with peaks that are enhanced by a factor of 10^4 relative to the standard ΛCDM power spectrum lead to microhalos that produce detectable brightness fluctuations when stars pass through the lensing caustics of galaxy clusters [42].

Our calculation of the small-scale power spectrum cut-off that results from the relativistic pressure yields a more accurate mapping between the properties of EMDE cosmologies and the observable signals that can help detect or constrain them. Our work thus improves our ability to probe the microscopic properties of hidden sectors and the expansion history of the early universe.

Acknowledgments

A   The evolution of the homogeneous hidden sector background

The Y particles that dominate the energy density of the universe during the EMDE are initially relativistic and transition to a pressureless state as the hidden sector temperature decreases. This appendix presents calculations for the evolution of the equation of state, pressure, and density of the Y particles.

A.1   Method

We use energy conservation and number density conservation to formulate a system of coupled differential equations for quantities related to the hidden sector temperature $T_{\rm hs}$ and the chemical potential of the Y particles, denoted by μ. We will assume here that the Y particle has g degrees of freedom and write the energy density ρ_Y, pressure P_Y, and number density n_Y as thermodynamic integrals:

$$\rho_Y(T_{\rm hs}, \mu) = \frac{g}{2\pi^2} \int_0^\infty \frac{E(p)}{e^{(E-\mu)/T_{\rm hs}} \pm 1} p^2 dp \, ; \tag{A.1a}$$

$$P_Y(T_{\rm hs}, \mu) = \frac{g}{6\pi^2} \int_0^\infty \frac{p^2}{E(p)} \frac{1}{e^{(E-\mu)/T_{\rm hs}} \pm 1} p^2 dp \, ; \tag{A.1b}$$

$$n_Y(T_{\rm hs}, \mu) = \frac{g}{2\pi^2} \int_0^\infty \frac{1}{e^{(E-\mu)/T_{\rm hs}} \pm 1} p^2 dp \, , \tag{A.1c}$$

where the ± 1 in the denominator denotes fermions (upper sign) or bosons (lower sign). These integrals can be expressed in terms of dimensionless quantities: $z \equiv p/T_{\rm hs}$, $x \equiv m/T_{\rm hs}$, $\Delta \equiv -\mu/T_{\rm hs}$, $\epsilon \equiv \frac{E}{T_{\rm hs}} = \frac{\sqrt{p^2+m^2}}{T_{\rm hs}} = \sqrt{z^2 + x^2}$ so that

$$\rho_Y(x, \Delta) = \frac{gm^4}{2\pi^2 x^4} \int_0^\infty \frac{z^2 \epsilon}{e^{(\epsilon+\Delta)} \pm 1} dz \, ; \tag{A.2a}$$

$$P_Y(x, \Delta) = \frac{gm^4}{6\pi^2 x^4} \int_0^\infty \frac{z^4 \epsilon^{-1}}{e^{(\epsilon+\Delta)} \pm 1} dz \, ; \tag{A.2b}$$

$$n_Y(x, \Delta) = \frac{gm^3}{2\pi^2 x^3} \int_0^\infty \frac{z^2}{e^{(\epsilon+\Delta)} \pm 1} dz. \tag{A.2c}$$

We also introduce the notation

$$J[f] \equiv \int_0^\infty \frac{z^2 f(z, x, \Delta)}{e^{(\epsilon+\Delta)} \pm 1} dz. \tag{A.3}$$

Conservation of energy density and number density imply

$$\dot{\rho}_Y + 3H(1 + w_Y)\rho_Y = 0 \, , \tag{A.4a}$$

$$\dot{n}_Y + 3Hn_Y = 0 \, , \tag{A.4b}$$

where $w_Y(x, \Delta) \equiv P_Y(x, \Delta)/\rho_Y(x, \Delta)$ and overdots denote proper time derivatives. Note that we have ignored the decay of the Y particles because an EMDE only occurs when the Y particles transition to nonrelativistic behavior well before they decay. To transform eqs. (A.4) into differential equations for x and Δ, we express $\dot{\rho}_Y$ and $\dot{n}_Y$ in terms of $\dot{x}$ and $\dot{\Delta}$. For ρ_Y, we have

$$\dot{\rho}_Y = \frac{gm^4}{2\pi^2 x^4} \left(R_1 \dot{x} - J\left[\frac{\epsilon e^{(\epsilon+\Delta)}}{e^{(\epsilon+\Delta)} \pm 1} \right] \dot{\Delta} \right), \tag{A.5}$$

where

$$R_1 = -\frac{4}{x} J[\epsilon] + xJ[\epsilon^{-1}] - xJ\left[\frac{e^{(\epsilon+\Delta)}}{e^{(\epsilon+\Delta)} \pm 1} \right]. \tag{A.6}$$

And similarly,

$$\dot{n}_Y = \frac{gm^3}{2\pi^2 x^3} \left(N_1 \dot{x} - J\left[\frac{e^{(\epsilon+\Delta)}}{e^{(\epsilon+\Delta)} \pm 1} \right] \dot{\Delta} \right), \tag{A.7}$$

where

$$N_1 = -\frac{3}{x} J[1] - xJ\left[\frac{e^{(\epsilon+\Delta)}}{\epsilon(e^{(\epsilon+\Delta)} \pm 1)} \right]. \tag{A.8}$$

Substituting these definitions in eqs. (A.4) and isolating $\dot{x}$ and $\dot{\Delta}$ yields

$$\dot{x} = \frac{3HN_0 R_2 - 3H(1 + w_Y)R_0 N_2}{R_1 N_2 - N_1 R_2} \, , \tag{A.9a}$$

$$\dot{\Delta} = \frac{3H(1 + w_Y)R_0 N_1 - 3HN_0 R_1}{R_1 N_2 - N_1 R_2}. \tag{A.9b}$$

Equations (A.9) are solved to obtain the hidden sector temperature $T_{\rm hs}$ and the chemical potential μ of the Y particles as a function of time. With $T_{\rm hs}$ and μ obtained, the time evolution of the Y particle density and pressure can be calculated using eqs. (A.1a) and (A.1b) respectively. Finally, the equation of state w_Y and the sound speed c_{sY}^2 can be computed; $w_Y = P_Y/\rho_Y$ and $c_{sY}^2 = \delta P_Y/\delta \rho_Y = P_Y'/\rho_Y' = w_Y - w_Y'/(3(1 + w_Y))$, where primes denote $d/d\ln a$.

A.2 Modeling the transition from relativistic to nonrelativistic behavior

The evolution of ρ_Y can be modeled by a broken power law with a pivot point a_p. Since the Y particles become nonrelativistic long before their comoving density is altered by their decays, an expression for a_p can be obtained by conserving $n_Y a^3$ through the transition from relativistic to nonrelativistic behavior.

We use the ansatz $a_p/a_i = bT_{\mathrm{hs,i}}/m$, where $T_{\mathrm{hs,i}}$ is the hidden sector temperature at a_i. Let us assume that the Y particles have become fully nonrelativistic at scale factor a_{nr}. Conserving particle number implies $n_Y(a_i)a_i^3 = n_Y(a_{\mathrm{nr}})a_{\mathrm{nr}}^3$. Since the Y particles are nonrelativistic at a_{nr}, we can write

$$\rho_Y(a_{\mathrm{nr}}) = mn_Y(a_{\mathrm{nr}}) = mn_Y(a_i)\frac{a_i^3}{a_{\mathrm{nr}}^3}. \tag{A.10}$$

Using the broken-power-law model for $\rho_Y(a)$, we can also express

$$\rho_Y(a_{\mathrm{nr}}) = \rho_Y(a_i)\left(\frac{a_i}{a_p}\right)^4\left(\frac{a_p}{a_{\mathrm{nr}}}\right)^3, \tag{A.11}$$

where we have used $\rho_Y(a) \propto a^{-4}$ for $a_i \leq a \leq a_p$ and $\rho_Y(a) \propto a^{-3}$ for $a_p \leq a \leq a_{\mathrm{nr}}$. At a_i, the Y particles are relativistic with a temperature $T_{\mathrm{hs,i}}$, therefore $n_Y(a_i) = gf'\zeta(3)T_{\mathrm{hs,i}}^3/\pi^2$ and $\rho_Y(a_i) = gf\pi^2 T_{\mathrm{hs,i}}^4/30$, where g is the degrees of freedom of the Y particles, f is 1 or 7/8 if the Y particles are bosons or fermions respectively, and f' is 1 if the Y particles are bosons and 3/4 if they are fermions. Equating the definitions of $\rho_Y(a_{\mathrm{nr}})$ from eqs. (A.10) and (A.11) and using the expressions for $n_Y(a_i)$ and $\rho_Y(a_i)$ from above with $a_p/a_i = bT_{\mathrm{hs,i}}/m$, we obtain

$$b = \frac{f}{f'}\frac{\pi^4}{30}\frac{1}{\zeta(3)}. \tag{A.12}$$

Substituting the values of f and f' yields $b = 2.70$ if the Y particles are bosons and $b = 3.15$ if they are fermions.

The evolution of w_Y and c_{sY}^2 can also be described by broken power laws. Both these quantities are equal to $1/3$ when the Y particles are relativistic and are proportional to a^{-2} when the Y particles become nonrelativistic. This behavior is illustrated for a case with $m = 1\,\mathrm{TeV}$ and $T_{\mathrm{hs,i}} = 200m$ by the blue solid curves in figure 18. We find that w_Y and c_{sY}^2 are well-described by the functional form

$$f(a, a_b, D) = \frac{1}{3}\left[1 + \left(\frac{a}{a_b}\right)^{\frac{1}{D}}\right]^{-2D}, \tag{A.13}$$

where a_b is the bending scale factor where the function transitions from the early-time power law to the late-time power law and D models the width of the transition.

Treating a_b and D as fit parameters, the numerical solutions for w_Y and c_{sY}^2 were fit to the above function for a range of masses and values of $T_{\mathrm{hs,i}}/m$ for both boson and fermion Y particles. The best fit values are presented in table 1. The orange dashed lines in figure 18 show the functions of the form given by eq. (A.13) with the best fit values of a_b and D given in table 1. The bottom panels show the relative error between the numerical solution and the best fit functions. The error stays within 1.5% for w_Y and 1.2% for c_{sY}^2 and stays within 0.2% at late times for both quantities.
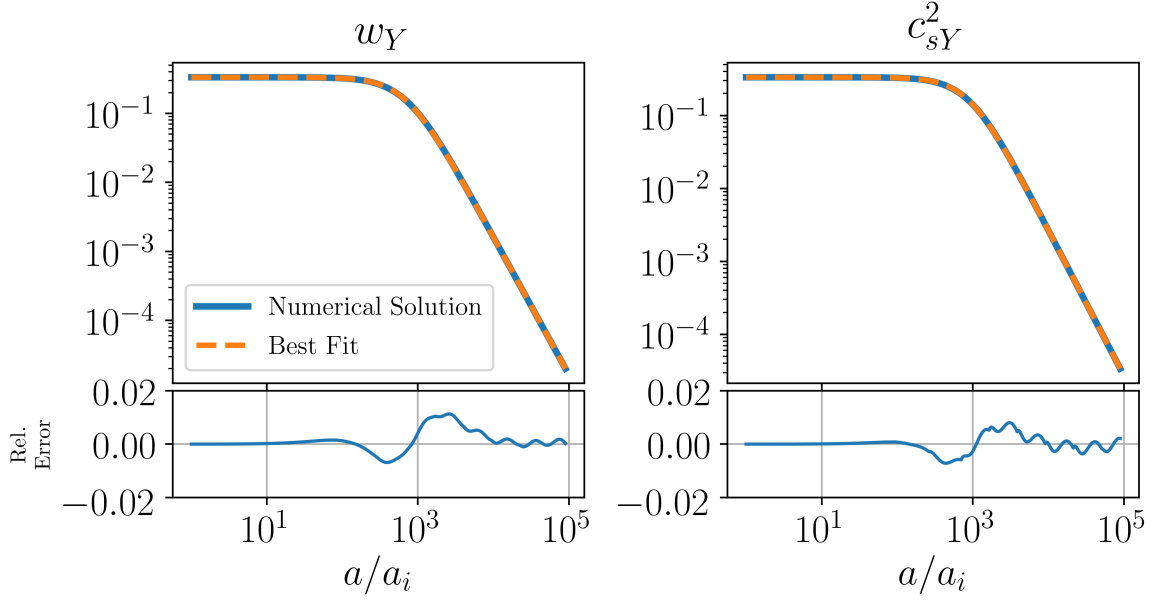
Figure 18. *Top*: numerical solutions and fitting functions for w_Y (left) and c^2_{sY} (right) for a fermion Y particle of $m = 1\,\mathrm{TeV}$ and $T_{\mathrm{hs}}(a_i) = 200m$. The fitting function curves use the best fit parameters given in table 1. *Bottom*: the relative error between the numerical solution and the fit function, given by $1 - \mathrm{Numerical/Fit}$.

Quantity	w_Y		c^2_{sY}	
	$(a_b/a_i)/(T_{\mathrm{hs,i}}/m)$	D	$(a_b/a_i)/(T_{\mathrm{hs,i}}/m)$	D
Boson Y	3.05	0.57	3.91	0.55
Fermion Y	3.49	0.56	4.48	0.54

Table 1. Best fit parameters for equation of state w_Y and sound speed c^2_{sY} for the functional form given by eq. (A.13).

We also used the fitting function for w_Y with the best fit parameters and integrated eq. (A.4a) to obtain ρ_Y to compare it with the numerical solution of ρ_Y. The relative error between the numerical and integrated ρ_Y peaks at 0.5% and stays constant at 0.2% at late times. Our fitting forms for w_Y can be used to obtain the time evolution of ρ_Y to within this error.

In the derivation of the peak wavenumber in section 4, we also use a piecewise model for c^2_{sY}, in which c^2_{sY} is approximated as a sharply broken power law with a pivot point, so that

$$
c^2_{sY} = \begin{cases} \frac{1}{3}, & a < a_{pc}, \\ \frac{1}{3}\frac{a^2_{pc}}{a^2}, & a > a_{pc}, \end{cases} \tag{A.14}
$$

with $a_{pc} = 1.43 a_p$ for bosonic Y particles and $a_{pc} = 1.41 a_p$ for fermionic Y particles, where a_p is the pivot scale factor for the evolution of $\rho_Y(a)$.

B   Relating the start of the EMDE to model parameters

In a universe that is initially dominated by relativistic SM particles, the EMDE starts when the energy density of the Y particles exceeds the energy density of the SM particles at a scale factor $a_{\rm dom}$, when the SM temperature is $T_{\rm dom}$. Here, we derive a few important expressions for quantities related to the start of the EMDE in terms of the parameters of our model: m (the Y particle mass), η (the ratio of the initial energy densities of SM radiation and the Y particles), the reheat temperature $T_{\rm RH}$ defined in eq. (2.3), and b, which is 2.70 and 3.15 if the Y particles are bosons and fermions, respectively. In the following, g denotes the degrees of freedom of the Y particles, and f is 1 or 7/8 for boson or fermion Y particles, respectively.

We first evaluate $a_{\rm dom}/a_p$, where a_p is the pivot scale factor for the broken power law followed by $\rho_Y(a)$. Since entropy is conserved for the SM radiation before the Y particle decays become significant, we have $g_*(T)a^3T^3 = {\rm constant}$, where we assume $g_*(T) = g_{*S}(T)$. As a result, $\rho_R \propto g_*(T(a))^{-1/3}a^{-4}$. Then,

$$\frac{\rho_R(a_p)}{\rho_{\rm dom}} = \frac{g_{\rm dom}^{1/3}a_{\rm dom}^4}{g_p^{1/3}a_p^4},\tag{B.1}$$

where $g_{\rm dom} = g_*(T_{\rm dom})$, $g_p = g_*(T(a_p))$ and $\rho_{\rm dom} = \rho_R(a_{\rm dom}) = \rho_Y(a_{\rm dom}) = (\pi^2/30)g_*(T_{\rm dom})T_{\rm dom}^4$. Furthermore, since $\rho_Y \propto a^{-3}$ from a_p to $a_{\rm dom}$, we can write

$$\frac{\rho_Y(a_p)}{\rho_{\rm dom}} = \frac{a_{\rm dom}^3}{a_p^3}.\tag{B.2}$$

Using eqs. (B.1) and (B.2), we have

$$\frac{\rho_R(a_p)}{\rho_Y(a_p)} = \left(\frac{g_{\rm dom}}{g_p}\right)^{\frac{1}{3}}\frac{a_{\rm dom}}{a_p}.\tag{B.3}$$

Similarly, we can express $\rho_R(a_p) = \rho_R(a_i)[g_i/g_p]^{1/3}[a_i/a_p]^4$, where $g_i = g_*(T_i)$. Since $\rho_Y \propto a^{-4}$ from a_i to a_p, $\rho_Y(a_p) = \rho_Y(a_i)[a_i/a_p]^4 = \eta^{-1}\rho_R(a_i)[a_i/a_p]^4$. Combining the previous two expressions yields

$$\frac{\rho_R(a_p)}{\rho_Y(a_p)} = \eta\left(\frac{g_i}{g_p}\right)^{\frac{1}{3}}.\tag{B.4}$$

Equating eqs. (B.3) and (B.4) gives us

$$\frac{a_{\rm dom}}{a_p} = \left(\frac{g_i}{g_{\rm dom}}\right)^{\frac{1}{3}}\eta.\tag{B.5}$$

The above relation can be used to express $T_{\rm dom}$ in terms of our model parameters. We can use $\rho_Y \propto a^{-4}$ from a_i to a_p and $\rho_Y \propto a^{-3}$ from a_p to $a_{\rm dom}$ to write

$$\rho_Y(a_{\rm dom}) = \rho_Y(a_i)\left(\frac{a_i}{a_p}\right)^4\left(\frac{a_p}{a_{\rm dom}}\right)^3.\tag{B.6}$$

According to our model for the evolution of $\rho_Y(a)$, $a_p/a_i = bT_{\rm hs,i}/m$ and $\rho_Y(a_i) = (\pi^2/30)gfT_{\rm hs,i}^4$. In addition, we use the expression for $a_{\rm dom}/a_p$ from eq. (B.5) and equate $\rho_Y(a_{\rm dom})$ to $(\pi^2/30)g_*(T_{\rm dom})T_{\rm dom}^4$ to obtain

$$g_{\text{dom}}^{\frac{1}{4}} T_{\text{dom}} = (gf)^{\frac{1}{4}} \left(\frac{g_i}{g_{\text{dom}}} \right)^{-\frac{1}{12}} \left(\frac{m}{b} \right) \eta^{-\frac{3}{4}}, \tag{B.7}$$

which gives

$$\rho_{\text{dom}} = gf \frac{\pi^2}{30} \left(\frac{g_i}{g_{\text{dom}}} \right)^{-\frac{1}{3}} \left(\frac{m}{b} \right)^4 \eta^{-3}. \tag{B.8}$$

Next, we derive an expression for $k_{\text{dom}}/k_{\text{RH}} \equiv (aH)_{a_{\text{dom}}}/(a_{\text{RH}}\Gamma)$. We divide eq. (B.5) by eq. (2.5) to get $a_{\text{dom}}/a_{\text{RH}}$, substitute Γ from eq. (2.3) and use ρ_{dom} from eq. (B.8) in $H(a_{\text{dom}}) = \sqrt{2(8\pi G/3)\rho_{\text{dom}}}$ to obtain

$$\frac{k_{\text{dom}}}{k_{\text{RH}}} = \sqrt{2} \left(\frac{gf}{g_*(T_{\text{RH}})} \right)^{\frac{1}{6}} \left(\frac{g_*(T_i)}{g_*(T_{\text{dom}})} \right)^{\frac{1}{6}} \left(\frac{(m/b)}{T_{\text{RH}}} \right)^{\frac{2}{3}} \eta^{-\frac{1}{2}}. \tag{B.9}$$

We also find it useful to derive an expression for $k/k_{\text{dom}} = (aH)_{a_k}/(aH)_{a_{\text{dom}}}$ for a mode k that enters the horizon at a_k during the period of radiation domination before the EMDE. Since the energy densities of the Y particles and the radiation are equal at a_{dom}, we have $H^2(a_{\text{dom}}) = 2 \times (8\pi G/3)\rho_R(a_{\text{dom}})$. It follows that

$$\frac{H(a_k)}{H(a_{\text{dom}})} = \frac{1}{\sqrt{2}} \left(\frac{g_{\text{dom}}}{g_k} \right)^{\frac{1}{6}} \left(\frac{a_{\text{dom}}}{a_k} \right)^2, \tag{B.10}$$

where $g_k = g_*(T(a_k))$, and

$$\frac{k}{k_{\text{dom}}} = \frac{1}{\sqrt{2}} \left(\frac{g_{\text{dom}}}{g_k} \right)^{\frac{1}{6}} \frac{a_{\text{dom}}}{a_k}. \tag{B.11}$$

Using eq. (B.11) with eq. (B.5) yields

$$\frac{k_p}{k_{\text{dom}}} = \left(\frac{g_i^2}{g_p g_{\text{dom}}} \right)^{\frac{1}{6}} \frac{\eta}{\sqrt{2}} \tag{B.12}$$

for a universe with $\eta > 1$.

Finally, we obtain an expression for $k_y/k_{\text{dom}} = a_y H(a_y)/(a_{\text{dom}} H(a_{\text{dom}}))$ where a_y is the scale factor at which $T_{\text{hs}} = m$. For this derivation, we relax the assumption of radiation domination before the EMDE because ρ_Y contributes significantly to $H(a_y)$ for $\eta \lesssim 10$. Since the Y particles are relativistic at a_y and $T_{\text{hs}} \propto a^{-1}$ for $a_i < a < a_y$, we can express $a_y = a_i T_{\text{hs,i}}/m = a_p/b$. Using eq. (B.5), this yields

$$\frac{a_{\text{dom}}}{a_y} = \left(\frac{g_i}{g_{\text{dom}}} \right)^{\frac{1}{3}} b\eta. \tag{B.13}$$

Next, we can express $H^2(a_y) = 8\pi G[\rho_Y(a_y) + \rho_R(a_y)]/3 = 8\pi G\rho_R(a_y)[1 + \eta^{-1}]/3$. Using the scaling $\rho_R(a) \propto g(T(a))^{-1/3}a^{-4}$ with the definition of ρ_{dom} from eq. (B.8) in $H^2(a_{\text{dom}}) = 16\pi G\rho_{\text{dom}}/3$, and the expression for a_{dom}/a_y from eq. (B.13), we obtain

$$\frac{k_y}{k_{\text{dom}}} = \left(\frac{g_i^2}{g_y g_{\text{dom}}} \right)^{\frac{1}{6}} \frac{b\eta\sqrt{1 + \eta^{-1}}}{\sqrt{2}}. \tag{B.14}$$

C Perturbation equations

We work in the Newtonian gauge:

$$ds^2 = -(1+2\psi)dt^2 + a^2(t)(1+2\phi)(dx^2 + dy^2 + dz^2). \tag{C.1}$$

Ignoring anisotropic stress, we have $\psi = -\phi$. In the absence of decays, the general equations for the density contrast $\delta \equiv (\rho - \bar{\rho})/\bar{\rho}$ and velocity dispersion $\theta \equiv a\partial_i dv^i/dt$ of a fluid for a Fourier mode k are [61]:

$$\delta' + (1+w)\frac{\theta}{aH} + 3(c_s^2 - w)\delta + 3(1+w)\phi' = 0\,,$$
$$\theta' + (1-3w)\theta + \frac{w'}{1+w}\theta - k^2\frac{c_s^2}{1+w}\frac{\delta}{aH} + k^2\frac{\phi}{aH} = 0\,, \tag{C.2}$$

where primes denote $d/d\ln a$, $w \equiv P/\rho$ is the ratio of the pressure and density of the fluid, and the sound speed is $c_s^2 \equiv \delta P/\delta\rho = P'/\rho' = w - w'/3(1+w)$.

The effects of Y particles decaying into SM radiation are incorporated into the perturbation equations as in ref. [32], which assumed a nonrelativistic Y particle. Their treatment can be used because w_Y is negligible in the epoch when the decay of the Y particles is significant, i.e. $\Gamma w_Y/H \approx 0$ at all times. The $\mathcal{O}(\Gamma w_Y/H)$ corrections to these equations are given in ref. [28]. The full coupled system of equations for the three fluids and gravity is

$$\delta'_X = -\frac{\theta_X}{aH} - 3\phi'\,; \tag{C.3a}$$

$$\theta'_X = -\theta_X - k^2\frac{\phi}{aH}\,; \tag{C.3b}$$

$$\delta'_Y = -(1+w_Y)\frac{\theta_Y}{aH} - 3(c_{sY}^2 - w_Y)\delta_Y - 3(1+w_Y)\phi' + \frac{\Gamma}{H}\phi\,; \tag{C.3c}$$

$$\theta'_Y = -(1-3w_Y)\theta_Y - \frac{w'_Y}{1+w_Y}\theta_Y + k^2\frac{c_{sY}^2}{1+w_Y}\frac{\delta_Y}{aH} - k^2\frac{\phi}{aH}\,; \tag{C.3d}$$

$$\delta'_R = -\frac{4}{3}\frac{\theta_R}{aH} - 4\phi' + \frac{\rho_Y}{\rho_R}\frac{\Gamma}{H}(\delta_Y - \delta_R - \phi)\,; \tag{C.3e}$$

$$\theta'_R = k^2\frac{\delta_R}{4aH} - k^2\frac{\phi}{aH} + \frac{\rho_Y}{\rho_R}\frac{\Gamma}{H}\left(\frac{3\theta_Y}{4} - \theta_R\right)\,; \tag{C.3f}$$

$$\phi' = -\left(1 + \frac{k^2}{3H^2a^2}\right)\phi + \frac{4\pi G}{3H^2}\left(\sum \delta_i\rho_i\right). \tag{C.3g}$$

To determine the initial conditions of the system given by eqs. (C.3), we first set $\phi(a = a_i) = \Phi_0$. We assume adiabatic perturbations and equate the primordial curvature perturbation for all three species:

$$\zeta_j = \Phi - \frac{\delta_j}{[\ln\rho_j]'}, \tag{C.4}$$

where j indicates each fluid. For superhorizon modes $\zeta = 3\Phi_0/2$ in a universe dominated by radiation or relativistic Y particles. Setting $\zeta_j = \zeta$ for each species, we have the initial

conditions,

$$\frac{\delta_R}{\Phi_0} = 2\,; \tag{C.5a}$$

$$\frac{\delta_X}{\Phi_0} = \frac{3}{2}\,; \tag{C.5b}$$

$$\frac{\delta_Y}{\Phi_0} = -\frac{1}{2}[\ln \rho_Y]'|_{a=a_i}, \tag{C.5c}$$

where a_i is the scale factor at which our calculations begin, chosen such that $T_{\text{hs}}(a_i) = 300m$. The initial conditions for the velocity dispersions are [61]

$$\theta_R = \theta_X = \theta_Y = -\frac{k^2 \Phi_0}{2H(a_i)}. \tag{C.6}$$

For a universe that is initially dominated by nonrelativistic Y particles, the initial conditions are similar to those in matter domination. For superhorizon modes, the primordial curvature perturbation is related to the metric perturbation as $\zeta_0 = 5\Phi_{0m}/3$. The primordial curvature perturbations for all species, given by eq. (C.4), are set equal to each other, yielding

$$\frac{\delta_R}{\Phi_{0m}} = 8/3\,; \tag{C.7a}$$

$$\frac{\delta_X}{\Phi_{0m}} = 2\,; \tag{C.7b}$$

$$\frac{\delta_Y}{\Phi_{0m}} = 2. \tag{C.7c}$$

The initial conditions for θ_i are given by eq. (C.6) with Φ_{0m} replacing Φ_0.

D EMDE power spectrum application

The EMDE modifies the matter power spectrum for modes that enter the horizon during or before the EMDE ($k > k_{\text{RH}}$). For an EMDE that results from cold Y particles dominating the universe after inflation, this modification to the power spectrum was described by ref. [29]. For $k < 0.05k_{\text{RH}}$, the power spectrum remains the same. For $k > 0.05k_{\text{RH}}$, $\delta(k) \to R(k)\delta(k)$, where

$$R(k) = \frac{A\left(\frac{k}{0.86k_{\text{RH}}}\right) \ln\left[\left(\frac{4}{e^3}\right)^{\frac{f_2}{f_1}} \frac{B\left(\frac{k}{0.86k_{\text{RH}}}\right)^{a_{\text{eq}}}}{a_k}\right]}{9.11 \ln\left[\left(\frac{4}{e^3}\right)^{\frac{f_2}{f_1}} 0.594\frac{\sqrt{2}k}{k_{\text{eq}}}\right]}. \tag{D.1}$$

In this equation, a_k is the scale factor of horizon entry for mode k and a_{eq} and k_{eq} are the scale factor and horizon wavenumber at matter-radiation equality, respectively. The values of f_1 and f_2 are determined by the baryon fraction $f_{\text{b}} \equiv \rho_{\text{bar}}/(\rho_{\text{b}} + \rho_{\text{matter}})$:

$$f_1 = 1 - 0.568f_{\text{b}} + 0.094f_{\text{b}}^2;$$
$$f_2 = 1 - 1.156f_{\text{b}} + 0.149f_{\text{b}}^2 - 0.074f_{\text{b}}^3.$$

Furthermore,

$$\frac{a_{\rm eq}}{a_k} = \frac{\sqrt{2}k}{k_{\rm eq}} \left[1 + \left(\frac{k}{k_{\rm RH}}\right)^{4.235}\right]^{1/4.235}, \tag{D.2}$$

and the fitting functions for A and B are:

$$A(x) = \exp\left[\frac{0.609}{\{1 + 2.15(\ln x - 1.52)^2\}^{1.38}}\right] \tag{D.3}$$
$$\times \left[9.11\,\mathcal{S}(5.02 - x) + \frac{3}{5}x^2\,\mathcal{S}(x - 5.02)\right];$$
$$\ln B(x) = \ln(0.594)\,\mathcal{S}(5.02 - x) + \ln\left(\frac{e}{x^2}\right)\mathcal{S}(x - 5.02),$$

where

$$\mathcal{S}(y) = \frac{1}{2}\left[\tanh\left(\frac{y}{2}\right) + 1\right] \tag{D.4}$$

models a step function.

If an epoch of SM radiation domination precedes the EMDE, modes with $k > k_{\rm dom}$ grow logarithmically with scale factor after entering the horizon and before the EMDE. This modifies $\delta(k > k_{\rm dom})$. From our fitting function for $\delta_{Y,c}(k > 10k_{\rm RH})$ given by eq. (5.7), we find that this modification is modeled by the scale-dependent factor

$$R_{\rm RD}(q) = \frac{\ln(1 + 0.22q)}{0.22q}[1 + 1.11q + (0.94q)^2 + (0.63q)^3 + (0.45q)^4]^{-1/4}, \tag{D.5}$$

where $q = k/k_{\rm dom}$ and $R_{\rm RD} = 1$ for $\eta < 1$. Finally, the small-scale cut-off can be imposed on $\delta(k)$ using our transfer functions $T(k) = \exp[-(k/k_{\rm cut})^n]$ from section 5. In summary, the combined effect of the EMDE, an epoch of radiation domination before the EMDE, and the small-scale cut-off due to the relativistic pressure of the Y particles modifies $\delta(k)$ by a factor

$$R_{\rm EMD}(k) = R(k)R_{\rm RD}(k)T(k). \tag{D.6}$$

The above expression for $R_{\rm EMD}(k)$ is valid at all times after the EMDE ends. We provide an online application for the easy computation and visualization of $R_{\rm EMD}$.[1] The calculations of the peak and cut-off scales in the application neglect the variation of g_*, the number of relativistic degrees of freedom in the SM radiation, before the EMDE. The parameters $T_{\rm RH}$, η and $k_{\rm dom}/k_{\rm RH}$ or $k_y/k_{\rm RH}$ can be varied by the user, and the output is downloadable as a table.

---

[1]https://hganjoo-emde-emde-rk-s7ww2v.streamlitapp.com/.

References

[1] LUX collaboration, *Results from a search for dark matter in the complete LUX exposure*, *Phys. Rev. Lett.* **118** (2017) 021303 [`arXiv:1608.07648`] [ɪɴSPIRE].

[2] PᴀɴᴅᴀX-II collaboration, *Dark matter results from 54-ton-day exposure of PandaX-II Experiment*, *Phys. Rev. Lett.* **119** (2017) 181302 [`arXiv:1708.06917`] [ɪɴSPIRE].

[3] XENON collaboration, *Dark matter search results from a one ton-year exposure of XENON1T*, *Phys. Rev. Lett.* **121** (2018) 111302 [`arXiv:1805.12562`] [ɪɴSPIRE].

[4] ATLAS collaboration, *Search for dark matter produced in association with bottom or top quarks in $\sqrt{s} = 13$ TeV pp collisions with the ATLAS detector*, *Eur. Phys. J. C* **78** (2018) 18 [`arXiv:1710.11412`] [ɪɴSPIRE].

[5] ATLAS collaboration, *Search for dark matter and other new phenomena in events with an energetic jet and large missing transverse momentum using the ATLAS detector*, *JHEP* **01** (2018) 126 [`arXiv:1711.03301`] [ɪɴSPIRE].

[6] ATLAS collaboration, *Search for dark matter in events with a hadronically decaying vector boson and missing transverse momentum in pp collisions at $\sqrt{s} = 13$ TeV with the ATLAS detector*, *JHEP* **10** (2018) 180 [`arXiv:1807.11471`] [ɪɴSPIRE].

[7] ATLAS collaboration, *Search for an invisibly decaying Higgs boson or dark matter candidates produced in association with a Z boson in pp collisions at $\sqrt{s} = 13$ TeV with the ATLAS detector*, *Phys. Lett. B* **776** (2018) 318 [`arXiv:1708.09624`] [ɪɴSPIRE].

[8] CMS collaboration, *Search for new physics in dijet angular distributions using proton-proton collisions at $\sqrt{s} = 13$ TeV and constraints on dark matter and other models*, *Eur. Phys. J. C* **78** (2018) 789 [*Erratum ibid.* **82** (2022) 379] [`arXiv:1803.08030`] [ɪɴSPIRE].

[9] CMS collaboration, *Search for dark matter in events with energetic, hadronically decaying top quarks and missing transverse momentum at $\sqrt{s} = 13$ TeV*, *JHEP* **06** (2018) 027 [`arXiv:1801.08427`] [ɪɴSPIRE].

[10] CMS collaboration, *Search for narrow and broad dijet resonances in proton-proton collisions at $\sqrt{s} = 13$ TeV and constraints on dark matter mediators and other new particles*, *JHEP* **08** (2018) 130 [`arXiv:1806.00843`] [ɪɴSPIRE].

[11] CMS collaboration, *Search for dark matter produced in association with a Higgs boson decaying to $\gamma\gamma$ or $\tau^+\tau^-$ at $\sqrt{s} = 13$ TeV*, *JHEP* **09** (2018) 046 [`arXiv:1806.04771`] [ɪɴSPIRE].

[12] CMS collaboration, *Search for top squarks and dark matter particles in opposite-charge dilepton final states at $\sqrt{s} = 13$ TeV*, *Phys. Rev. D* **97** (2018) 032009 [`arXiv:1711.00752`] [ɪɴSPIRE].

[13] CMS collaboration, *Search for dark matter particles produced in association with a top quark pair at $\sqrt{s} = 13$ TeV*, *Phys. Rev. Lett.* **122** (2019) 011803 [`arXiv:1807.06522`] [ɪɴSPIRE].

[14] M. Pospelov, A. Ritz and M.B. Voloshin, *Secluded WIMP Dark Matter*, *Phys. Lett. B* **662** (2008) 53 [`arXiv:0711.4866`] [ɪɴSPIRE].

[15] N. Arkani-Hamed, D.P. Finkbeiner, T.R. Slatyer and N. Weiner, *A theory of dark matter*, *Phys. Rev. D* **79** (2009) 015014 [`arXiv:0810.0713`] [ɪɴSPIRE].

[16] D. Hooper, N. Weiner and W. Xue, *Dark forces and light dark matter*, *Phys. Rev. D* **86** (2012) 056009 [`arXiv:1206.2929`] [ɪɴSPIRE].

[17] A. Berlin, P. Gratia, D. Hooper and S.D. McDermott, *Hidden sector dark matter models for the galactic center gamma-ray excess*, *Phys. Rev. D* **90** (2014) 015032 [`arXiv:1405.5204`] [ɪɴSPIRE].

[18] M. Abdullah, A. DiFranzo, A. Rajaraman, T.M.P. Tait, P. Tanedo and A.M. Wijangco, *Hidden on-shell mediators for the Galactic Center γ-ray excess*, *Phys. Rev. D* **90** (2014) 035004 [`arXiv:1404.6528`] [ɪɴSPIRE].

[19] A. Martin, J. Shelton and J. Unwin, *Fitting the galactic center gamma-ray excess with cascade annihilations*, *Phys. Rev. D* **90** (2014) 103513 [`arXiv:1405.0272`] [ɪɴSPIRE].

[20] X. Chen and S.H.H. Tye, *Heating in brane inflation and hidden dark matter*, *JCAP* **06** (2006) 011 [`hep-th/0602136`] [InSPIRE].

[21] Y. Zhang, *Long-lived light mediator to dark matter and primordial small scale spectrum*, *JCAP* **05** (2015) 008 [`arXiv:1502.06983`] [InSPIRE].

[22] A. Berlin, D. Hooper and G. Krnjaic, *PeV-scale dark matter as a thermal relic of a decoupled sector*, *Phys. Lett. B* **760** (2016) 106 [`arXiv:1602.08490`] [InSPIRE].

[23] A. Berlin, D. Hooper and G. Krnjaic, *Thermal dark matter from a highly decoupled sector*, *Phys. Rev. D* **94** (2016) 095019 [`arXiv:1609.02555`] [InSPIRE].

[24] J.A. Dror, E. Kuflik and W.H. Ng, *Codecaying dark matter*, *Phys. Rev. Lett.* **117** (2016) 211801 [`arXiv:1607.03110`] [InSPIRE].

[25] J.A. Dror, E. Kuflik, B. Melcher and S. Watson, *Concentrated dark matter: enhanced small-scale structure from codecaying dark matter*, *Phys. Rev. D* **97** (2018) 063524 [`arXiv:1711.04773`] [InSPIRE].

[26] A.L. Erickcek, P. Ralegankar and J. Shelton, *Cannibal domination and the matter power spectrum*, *Phys. Rev. D* **103** (2021) 103508 [`arXiv:2008.04311`] [InSPIRE].

[27] R. Allahverdi et al., *The first three seconds: a review of possible expansion histories of the early universe*, `arXiv:2006.16182` [InSPIRE].

[28] A.L. Erickcek, P. Ralegankar and J. Shelton, *Cannibalism's lingering imprint on the matter power spectrum*, *JCAP* **01** (2022) 017 [`arXiv:2106.09041`] [InSPIRE].

[29] A.L. Erickcek and K. Sigurdson, *Reheating effects in the matter power spectrum and implications for substructure*, *Phys. Rev. D* **84** (2011) 083503 [`arXiv:1106.0536`] [InSPIRE].

[30] G. Barenboim and J. Rasero, *Structure formation during an early period of matter domination*, *JHEP* **04** (2014) 138 [`arXiv:1311.4034`] [InSPIRE].

[31] J. Fan, O. Özsoy and S. Watson, *Nonthermal histories and implications for structure formation*, *Phys. Rev. D* **90** (2014) 043536 [`arXiv:1405.7373`] [InSPIRE].

[32] A.L. Erickcek, *The dark matter annihilation boost from low-temperature reheating*, *Phys. Rev. D* **92** (2015) 103505 [`arXiv:1504.03335`] [InSPIRE].

[33] A.L. Erickcek, K. Sinha and S. Watson, *Bringing isolated dark matter out of isolation: late-time reheating and indirect detection*, *Phys. Rev. D* **94** (2016) 063502 [`arXiv:1510.04291`] [InSPIRE].

[34] C. Blanco, M.S. Delos, A.L. Erickcek and D. Hooper, *Annihilation signatures of hidden sector dark matter within early-forming microhalos*, *Phys. Rev. D* **100** (2019) 103010 [`arXiv:1906.00010`] [InSPIRE].

[35] M. Sten Delos, T. Linden and A.L. Erickcek, *Breaking a dark degeneracy: the gamma-ray signature of early matter domination*, *Phys. Rev. D* **100** (2019) 123546 [`arXiv:1910.08553`] [InSPIRE].

[36] N. Blinov, M.J. Dolan, P. Draper and J. Shelton, *Dark matter microhalos from simplified models*, *Phys. Rev. D* **103** (2021) 103514 [`arXiv:2102.05070`] [InSPIRE].

[37] Y. Bai and J. Berger, *Lepton portal dark matter*, *JHEP* **08** (2014) 153 [`arXiv:1402.6696`] [InSPIRE].

[38] C.P. Burgess, M. Pospelov and T. ter Veldhuis, *The minimal model of nonbaryonic dark matter: a singlet scalar*, *Nucl. Phys. B* **619** (2001) 709 [`hep-ph/0011335`] [InSPIRE].

[39] C. Bird, R.V. Kowalewski and M. Pospelov, *Dark matter pair-production in b —> s transitions*, *Mod. Phys. Lett. A* **21** (2006) 457 [`hep-ph/0601090`] [InSPIRE].

[40] W. Krolikowski, *A hidden valley model of cold dark matter with photonic portal*, `arXiv:0803.2977` [InSPIRE].

[41] M.S. Delos, M. Bruff and A.L. Erickcek, *Predicting the density profiles of the first halos*, *Phys. Rev. D* **100** (2019) 023523 [`arXiv:1905.05766`] [InSPIRE].

[42] N. Blinov, M.J. Dolan, P. Draper and J. Shelton, *Dark matter microhalos from simplified models*, *Phys. Rev. D* **103** (2021) 103514 [arXiv:2102.05070] [INSPIRE].

[43] C. Dvorkin, K. Blum and M. Kamionkowski, *Constraining dark matter-baryon scattering with linear cosmology*, *Phys. Rev. D* **89** (2014) 023519 [arXiv:1311.2937] [INSPIRE].

[44] W. Hu and N. Sugiyama, *Small scale cosmological perturbations: an analytic approach*, *Astrophys. J.* **471** (1996) 542 [astro-ph/9510117] [INSPIRE].

[45] W.H. Press and P. Schechter, *Formation of galaxies and clusters of galaxies by selfsimilar gravitational condensation*, *Astrophys. J.* **187** (1974) 425 [INSPIRE].

[46] M.S. Delos, *Tidal evolution of dark matter annihilation rates in subhalos*, *Phys. Rev. D* **100** (2019) 063505 [arXiv:1906.10690] [INSPIRE].

[47] M.S. Delos, *Evolution of dark matter microhalos through stellar encounters*, *Phys. Rev. D* **100** (2019) 083529 [arXiv:1907.13133] [INSPIRE].

[48] X. Shen, H. Xiao, P.F. Hopkins and K.M. Zurek, *Disruption of dark matter minihaloes in the milky way environment: implications for axion miniclusters and early matter domination*, arXiv:2207.11276 [INSPIRE].

[49] FERMI-LAT collaboration, *The spectrum of isotropic diffuse gamma-ray emission between 100 MeV and 820 GeV*, *Astrophys. J.* **799** (2015) 86 [arXiv:1410.3696] [INSPIRE].

[50] C. Blanco and D. Hooper, *Constraints on decaying dark matter from the isotropic gamma-ray background*, *JCAP* **03** (2019) 019 [arXiv:1811.05988] [INSPIRE].

[51] G. Steigman, B. Dasgupta and J.F. Beacom, *Precise relic WIMP abundance and its impact on searches for dark matter annihilation*, *Phys. Rev. D* **86** (2012) 023506 [arXiv:1204.3622] [INSPIRE].

[52] R. Allahverdi and J.K. Osiński, *Freeze-in production of dark matter prior to early matter domination*, *Phys. Rev. D* **101** (2020) 063503 [arXiv:1909.01457] [INSPIRE].

[53] G.F. Giudice, E.W. Kolb and A. Riotto, *Largest temperature of the radiation era and its cosmological implications*, *Phys. Rev. D* **64** (2001) 023508 [hep-ph/0005123] [INSPIRE].

[54] V.S.H. Lee, A. Mitridate, T. Trickle and K.M. Zurek, *Probing small-scale power spectra with pulsar timing arrays*, *JHEP* **06** (2021) 028 [arXiv:2012.09857] [INSPIRE].

[55] M.S. Delos and T. Linden, *Dark matter microhalos in the solar neighborhood: pulsar timing signatures of early matter domination*, *Phys. Rev. D* **105** (2022) 123514 [arXiv:2109.03240] [INSPIRE].

[56] H. Ramani, T. Trickle and K.M. Zurek, *Observability of dark matter substructure with pulsar timing correlations*, *JCAP* **12** (2020) 033 [arXiv:2005.03030] [INSPIRE].

[57] M. Oguri, J.M. Diego, N. Kaiser, P.L. Kelly and T. Broadhurst, *Understanding caustic crossings in giant arcs: characteristic scales, event rates, and constraints on compact dark matter*, *Phys. Rev. D* **97** (2018) 023518 [arXiv:1710.00148] [INSPIRE].

[58] J.M. Diego et al., *Dark matter under the microscope: constraining compact dark matter with caustic crossing events*, *Astrophys. J.* **857** (2018) 25 [arXiv:1706.10281] [INSPIRE].

[59] L. Dai and J. Miralda-Escudé, *Gravitational lensing signatures of axion dark matter minihalos in highly magnified stars*, *Astron. J.* **159** (2020) 49 [arXiv:1908.01773] [INSPIRE].

[60] G. Barenboim, N. Blinov and A. Stebbins, *Smallest remnants of early matter domination*, *JCAP* **12** (2021) 026 [arXiv:2107.10293] [INSPIRE].

[61] C.-P. Ma and E. Bertschinger, *Cosmological perturbation theory in the synchronous and conformal Newtonian gauges*, *Astrophys. J.* **455** (1995) 7 [astro-ph/9506072] [INSPIRE].